

1 **From Sugar to Flowers: A Transition of Shallow**
2 **Cumulus Organization During ATOMIC**

3 **Pornampai Narenpitak^{1,2}, Jan Kazil^{1,2}, Takanobu Yamaguchi^{1,2}, Patricia**
4 **Quinn³, Graham Feingold²**

5 ¹Cooperative Institute for Research in Environmental Sciences, University of Colorado Boulder, Boulder,
6 Colorado, USA

7 ²National Oceanic and Atmospheric Administration, Chemical Sciences Laboratory, Boulder, Colorado,
8 USA

9 ³National Oceanic and Atmospheric Administration, Pacific Marine Environmental Laboratory, Seattle,
10 Washington, USA

11 **Key Points:**

- 12 • Lagrangian LES can reproduce the transition of shallow cumulus organization from
13 sugar to flowers observed on Feb 2-3, 2020 during ATOMIC
- 14 • While large-scale upward vertical wind deepens the cloud layer, mesoscale wind
15 renders moist areas moister assisting cloud organization
- 16 • Stronger large-scale upward motion strengthens the mesoscale circulation and ac-
17 celerates the sugar-to-flowers transition process

Abstract

The Atlantic Tradewind Ocean-Atmosphere Mesoscale Interaction Campaign (ATOMIC) took place in January–February, 2020. It was designed to understand the relationship between shallow convection and the large-scale environment in the trade-wind regime. A Lagrangian large eddy simulation, following the trajectory of a boundary-layer airmass, can reproduce a transition of trade cumulus organization from “sugar” to “flower” clouds with cold pools, observed on February 2–3. The simulation is driven with reanalysis large-scale meteorology and ATOMIC in-situ aerosol data. During the transition, large-scale upward motion deepens the cloud layer. The total water path and optical depth increase, especially in the moist regions where flowers aggregate. This is due to mesoscale circulation that renders a net convergence of total water in the already moist and cloudy regions, strengthening the organization. An additional simulation shows that stronger large-scale upward motion reinforces the mesoscale circulation and accelerates the organization process by strengthening the cloud-layer mesoscale buoyant turbulence kinetic energy production.

Plain Language Summary

Fair-weather shallow clouds have different sizes and cloud properties. A field study called the Atlantic Tradewind Ocean-Atmosphere Mesoscale Interaction Campaign (ATOMIC) and Elucidating the Role of Clouds-Circulation Coupling in Climate (EUREC⁴A) was designed to further understand the properties of these clouds. On February 2–3, very small and shallow “sugar” clouds grow into wider and deeper “flower” cloud clusters, no more than 3 km high. The clear spaces between the clouds expand. This study finds that local air circulation is responsible for making the moist and cloudy areas moister, and dry and cloud-free areas drier, enabling a process responsible for this transition. The large-scale vertical winds modulate the rate and strength of this process which occurs locally at smaller scales.

1 Introduction

Low-level clouds forming in the warm marine boundary layer continue to be a leading source of uncertainty in global climate models (i.e. Bony & Dufresne, 2005; Boucher et al., 2013; Zelinka et al., 2016). Challenges associated with the study of these clouds include resolving the internal cloud processes at a fine scale while maintaining an accu-

49 rate representation of the meteorology in which the clouds occur. The time scale and sea-
50 sonality are also important, as summertime and wintertime shallow cumuli observed from
51 the same oceanic regions may exhibit different characteristics (Nuijens et al., 2014; Lamer
52 et al., 2015; Nuijens et al., 2015; Vogel et al., 2020).

53 Previous studies have used high-resolution simulations and satellite retrievals to
54 help understand the relationships between shallow cumulus properties and the large-scale
55 atmospheric and oceanic conditions. For example, the Barbados Oceanographic and Me-
56 teorological Experiment (BOMEX) examined the turbulent dynamics of summertime shal-
57 low cumuli in the Atlantic Ocean using different large eddy simulation (LES) models (Holland
58 & Rasmusson, 1973; Siebesma et al., 2003). The Cloud Feedback Model Intercompar-
59 ison Project—Global Atmospheric System Study Intercomparison of Large Eddy Mod-
60 els and Single Column Models (CGILS) investigated the mechanisms of cloud feedback
61 of shallow cumulus and stratocumulus under idealized climate change perturbations based
62 on summertime subtropical atmospheric conditions in the Pacific Ocean (Zhang et al.,
63 2013; Bretherton et al., 2013; Blossey et al., 2013). Bretherton and Blossey (2017) (re-
64 ferred to as BB2017 for short) further explored a mechanism of shallow cumulus organ-
65 ization in different large-scale conditions, including those from BOMEX and one of the
66 CGILS cases. Organization of precipitating shallow cumulus clouds in the presence of
67 cold pools during the Rain in Cumulus over the Ocean (RICO) (Rauber et al., 2007) has
68 been studied with LES by Seifert and Heus (2013), Zuidema et al. (2017), and the ref-
69 erences therein. In addition, Mieslinger et al. (2019) examined how different meteorolo-
70 gical conditions affect cloud properties across different oceanic basins using high-resolution
71 satellite imagery.

72 Other studies have used LES models to explore cloud processes that require finer
73 representation of shallow cumuli. For instance, Vial et al. (2019) found that the cloudi-
74 ness of wintertime North Atlantic trade shallow cumuli is sensitive to the diurnal cycle,
75 both for nonprecipitating and precipitating clouds. Vogel et al. (2020) found that trade
76 cumuli with stratiform cloudiness forming downstream of the trade wind region are tightly
77 controlled by the inversion strength, deepening of the cloud layer, and longwave radia-
78 tive cooling. Narenpitak and Bretherton (2019) used LES with forcings derived from the
79 trade wind region of an idealized aquaplanet cloud-resolving model to explore the response
80 of shallow cumulus in a warmer climate, and found that radiative cooling and free-tropospheric
81 humidity are keys to controlling the cloudiness in their simulations. The use of in-situ

82 observations, high-resolution simulations and remote sensing tools over the years have
83 enabled studies that lead to better understanding of shallow cumulus processes.

84 A field campaign designed to study shallow convection in the trade wind region oc-
85 curred in January–February, 2020 in the Atlantic Ocean east of Barbados. The Atlantic
86 Tradewind Ocean–Atmosphere Mesoscale Interaction Campaign (ATOMIC) and its Eu-
87 ropean counterpart, the European field campaign called Elucidating the Role of Clouds-
88 Circulation Coupling in Climate (EUREC⁴A), formed a field campaign that used instru-
89 ments on research aircrafts and ships to observe the properties of shallow cumulus clouds
90 in order to better understand their relationship with the large-scale environment (Quinn
91 et al., 2020; Pincus et al., 2021; Stevens et al., 2021). Recent studies (i.e. Stevens et al.,
92 2020; Rasp et al., 2020; Bony et al., 2020) have categorized the mesoscale organization
93 of shallow cumuli based on the Moderate Resolution Imaging Spectroradiometer (MODIS)
94 imagery into four types: sugar, gravel, fish, and flowers. Different states of organization
95 have different cloud properties including boundary layer depth, amount of precipitation,
96 cloud fraction, and cloud radiative effect.

97 On February 2–3, 2020, a transition from small and shallow clouds called “sugar”
98 to larger and deeper clouds called “flowers” occurred over the field campaign region (Fig.
99 1a; animation in Movie S1 in the Supporting Information (SI)). Backward trajectories
100 following the air mass at 500 m altitude show that these flower clouds originated from
101 a shallow sugar cloud layer northeast of National Oceanic and Atmospheric Administra-
102 tion’s (NOAA) Research Vessel Ronald H. Brown (RHB). Larger flowers with cold pools
103 were observed to the southwest, closer to Barbados. This study uses a Lagrangian LES,
104 with the domain following a boundary-layer trajectory (red box and yellow dots in Fig.
105 1a), to simulate this organization event. To understand the relationship between the large-
106 scale vertical velocity and the transition of the mesoscale organization, an additional LES
107 with modified large-scale vertical velocity is included.

108 The structure of this paper is as follows. Section 2 describes the simulation con-
109 figurations and the observations used to initialize the simulations. Section 3 shows the
110 transition from sugar to flowers represented by the LES. Section 4 discusses the mech-
111 anisms that are important for the organization. Section 5 identifies the role of large-scale
112 vertical motion on the sugar-to-flowers transition and the circulation at the mesoscale.

113 Finally, conclusions are given in Section 6. Appendices A through D are found at the
114 end of the manuscript. Movies S1-S3 are found in the SI.

115 **2 Data and Simulations**

116 The System for Atmospheric Modeling (SAM) (Khairoutdinov & Randall, 2003)
117 is employed. The large-scale meteorology and forcings of the simulations are derived from
118 the European Centre for Medium-Range Weather Forecasts (ECMWF) Reanalysis 5th
119 Generation (ERA5) (Hersbach et al., 2020), following the airmass at 500 m altitude through
120 the location of the RHB (54.5°W and 13.9°N) at 17 UTC on February 2. The airmass
121 trajectory was calculated by the Hybrid Single-Particle Lagrangian Integrated Trajec-
122 tory (HYSPLIT) model (Stein et al., 2015; Rolph et al., 2017) in the ERA5 pressure-
123 level data. The large-scale meteorology along the trajectory is, however, from the model-
124 level data. This makes use of ERA5’s full 137 vertical levels, especially for the vertical
125 velocity forcings. The horizontal winds are nudged toward ERA5 with Newtonian relax-
126 ation, with a 30 min time scale. Since the trajectory moves approximately with the bound-
127 ary layer, large-scale horizontal advection of the temperature and humidity is not included.
128 Instead, to account for horizontal advection in the free troposphere, the temperature and
129 humidity profiles of the simulation are nudged toward ERA5 with a 30 min relaxation
130 time scale. The temperature and humidity nudging begins 100 m above the inversion,
131 defined as the height of maximum vertical gradient of liquid water static energy in SAM
132 (or of liquid water potential temperature in ERA5, whichever is higher). From this nudg-
133 ing base level, the nudging tendencies increase smoothly over a height interval of 500 m
134 from a value of zero to a value corresponding to the nudging. The surface fluxes are cal-
135 culated by SAM based on the horizontal wind speeds nudged toward ERA5, and the tem-
136 perature and humidity profiles calculated by SAM in the boundary layer. Figure 1b-e
137 shows that at the times when the trajectory is within 1-degree distance from the RHB,
138 the outputs from SAM are consistent with the RHB radiosondes.

139 **2.1 Simulations**

140 The control simulation (CTL) is configured with 100 m horizontal grid spacing and
141 a horizontal domain extent of 192×192 km². The vertical grid spacing is 50 m, increas-
142 ing geometrically from 5 km to the domain top at 8 km (total of 120 levels). Above that,
143 the atmospheric profiles from ERA5 are used up to the top of the atmosphere for the

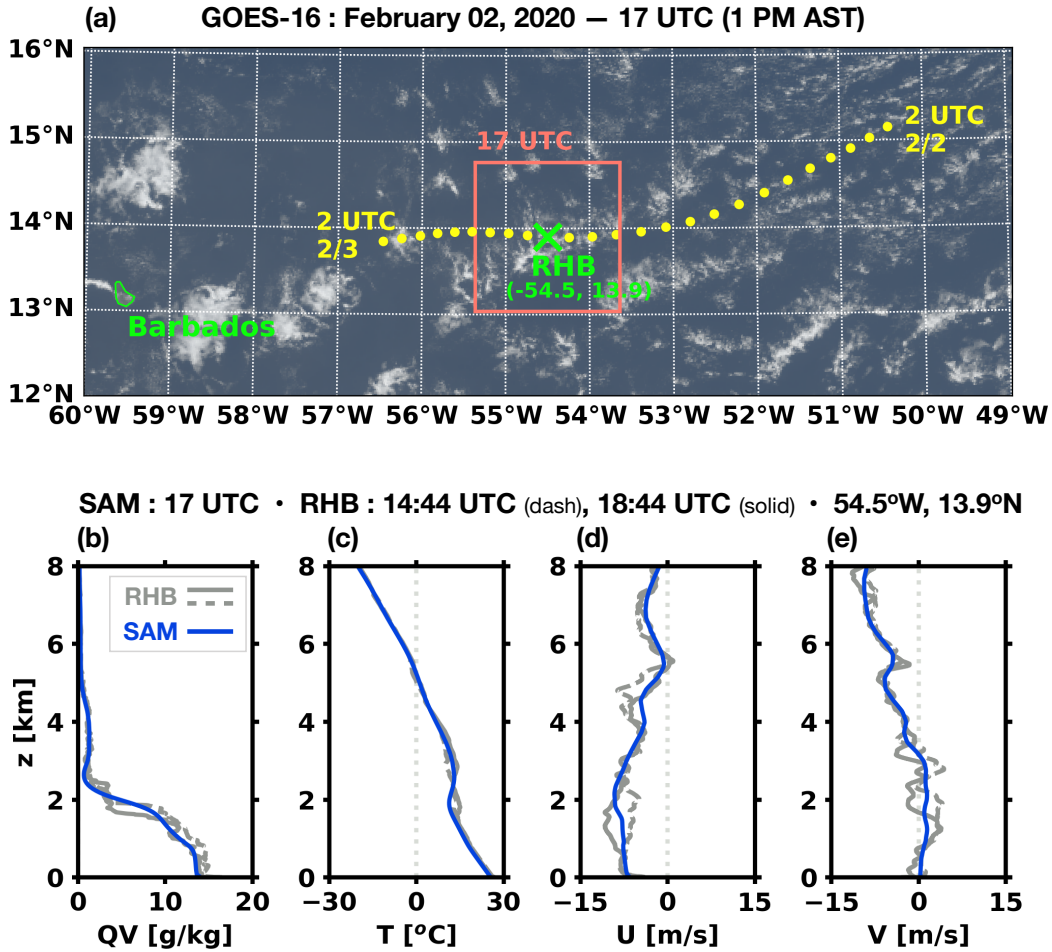


Figure 1. (a) A satellite image from the Geostationary Operational Environmental Satellite-16 (GOES-16) on February 2, 2020. The yellow dots represent hourly coordinates of the airmass following trajectory on which the Lagrangian simulations are based. The red box indicates the simulation’s $192 \times 192 \text{ km}^2$ domain extent, centered on the Research Vessel Ronald H. Brown (RHB, green ‘x’) at 17 UTC. (b-e) The comparisons between radiosondes from the RHB (grey) and domain-mean profiles from the System for Atmospheric Modeling (SAM) control simulation (blue) of the following variables: water vapor mixing ratio (QV), temperature (T), zonal wind (U) and meridional wind (V). The RHB radiosondes are taken at 14:44 UTC and 18:44 UTC, during which time the RHB is within SAM’s domain.

144 radiation calculation. The simulation uses a bulk two-moment (bin-emulating) micro-
 145 physics scheme (Feingold et al., 1998) and the Rapid Radiative Transfer Model for global
 146 climate model applications (RRTMG) (Mlawer et al., 1997) with time varying atmospheric
 147 profiles above the domain top and the diurnal cycle of solar radiation. The radiation is
 148 computed every 10 seconds. The model’s time step is 2 seconds, and the duration of the
 149 simulation is 24 hours, from 2 UTC on February 2 to 2 UTC on February 3, 2020.

150 An additional simulation called WeakW is performed using the same model con-
 151 figuration as CTL, except with a modified vertical velocity (W) in the forcings. The W
 152 profiles for WeakW are 50% weaker than CTL during a period with strong upward mo-
 153 tion, between 11 UTC and 19 UTC. Since SAM linearly extrapolates the hourly W forc-
 154 ing profiles to the model’s time step, W in WeakW diverges from CTL at 10 UTC, and
 155 converges again at 20 UTC (Fig. 3b-c).

156 2.2 The Initialization of Aerosol

157 There are two types of aerosol in the simulations: sea salt and mineral dust. Sea
 158 salt is included as it is the dominant non-dust aerosol type during for particles with di-
 159 ameters smaller than $10\mu\text{m}$, based on the shipboard measurement from the RHB (Quinn
 160 et al., 2020). Mineral dust was also present in the free troposphere east of Barbados dur-
 161 ing this time. The RHB radiometer measurements, together with the surface aerosol mea-
 162 surements, indicated the presence of scattering and absorbing aerosol in the free tropo-
 163 sphere. (Quinn et al., 2020). Visual observation during flights of the ATOMIC field cam-
 164 paign confirmed the presence of such aerosol above the cloud tops. Therefore, sea salt
 165 and mineral dust are initialized at the beginning of the simulation and allowed to ad-
 166 vect vertically by large-scale vertical velocity, and horizontally within the domain by trajectory-
 167 relative horizontal winds throughout the simulation. The sea-salt particles interact with
 168 the cloud microphysics scheme, while the mineral dust is coupled with the radiation scheme.
 169 See Appendix A for details on the initialization of the aerosol species.

170 3 Transition of Shallow Cumuli: From Sugar to Flowers

171 Simulation CTL is able to reproduce the transition from sugar to flowers on Febru-
 172 ary 2–3, 2020. Figure 2a-e shows $192\times 192\text{ km}^2$ snapshots from GOES-16 along the tra-
 173 jectory on which the simulation is based. Figure 2f-j and Movie S2 show the cloud state

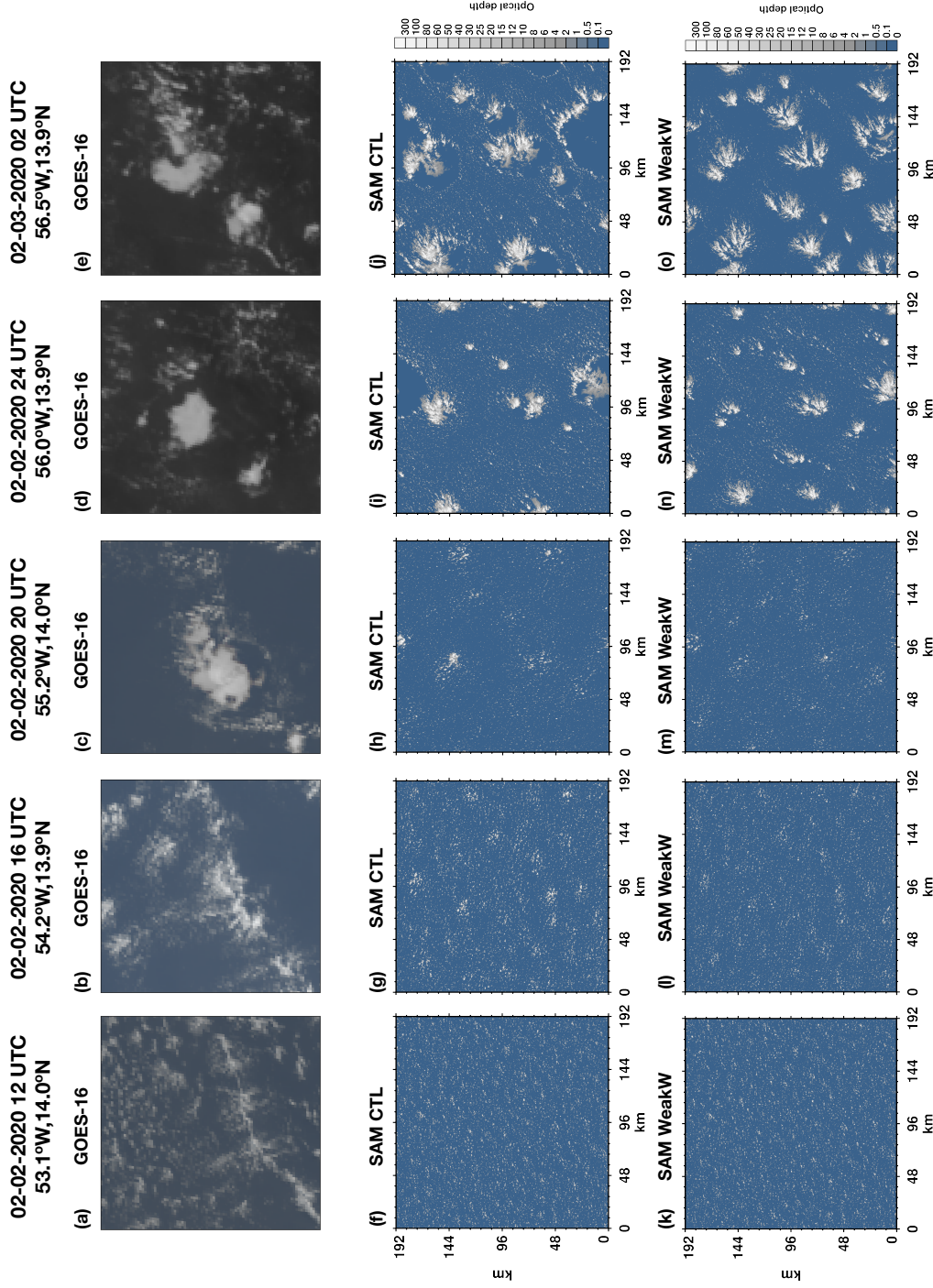


Figure 2. Comparisons of GOES-16 and SAM simulations over a $192 \times 192 \text{ km}^2$ domain at 12, 16, 20, and 24 UTC on February 2, and 2 UTC on February 3, 2020. (a-e) Satellite images from GOES-16, centered on the trajectory presented in Figure 1. (f-j) Snapshots of total (cloud+rain) optical depth from SAM control simulation (CTL). (k-o) As in Panels (f-j) but for the weaker vertical velocity simulation (WeakW).

174 evolution from CTL. A comparison between the snapshots from GOES-16 and CTL shows
175 that SAM reproduces the nature of the transition well, although there are some disagree-
176 ments between the satellite images and the simulation. In particular, the satellite im-
177 agery shows greater variability in cloud structure over the same area compared to the
178 simulation domain.

179 The sugar-to-flowers transition in CTL occurs between 8 UTC and 18 UTC, con-
180 sistent with GOES-16 except the satellite shows larger cloud clusters forming along a
181 line toward the south. During this time, the sugar cloud fields in CTL develop into con-
182 tiguous aggregates and expand laterally to mature into flowers. As the initial sugar clouds
183 organize, some interspersed cumulus clouds are suppressed while the ones that have ag-
184 gregated persist and grow. After 24 UTC the simulated cloud clusters expand and catch
185 up with those captured by GOES-16. The aggregated flowers in CTL produce precip-
186 itation, which partially evaporates before reaching the surface, resulting in cold down-
187 drafts that produce cold pools adjacent to the flowers.

188 Potential reasons for the discrepancy between SAM and GOES-16 could result from
189 disagreements in ERA5 profiles and sea surface temperature, and the model physics. Fur-
190 thermore, unlike regional models, SAM (and other LES) represent conditions at one par-
191 ticular location rather than the entire region of the satellite images. SAM operates with
192 spatially invariant top, bottom, and lateral boundary conditions, the latter of which are
193 periodic. However, in reality the area covered by the simulation domain experiences spa-
194 tial variability in boundary conditions, and lateral boundary conditions are not periodic.
195 Hence, we expect variability in the simulations to be smaller compared to reality over
196 the simulated area, with the simulation capturing the real cloud state only within a lim-
197 ited sub-region of the area seen in the satellite imagery. Nonetheless, the mean states
198 from SAM are still consistent with the observations, as shown in Figure 1b-e. Because
199 the simulation still faithfully captures the general nature of this transition as seen in the
200 satellite, the analysis is representative of what happens in reality.

201 **3.1 Multiscale Partitioning**

202 Although the simulations are run at 100 m grid spacing, it is helpful to coarse-grain
203 the outputs into larger tiles. This approach partitions the results into contributions from
204 the large-scale, mesoscale, and cumulus-scale processes (BB2017). Coarse-graining fil-

ters out the details at the smaller scales that may be associated with shallow convection but are not relevant to the organization. Similar to the approach taken by Honnert et al. (2011), the variance of total water path is computed at different scales (Appendix B). Total water path (TWP) is defined as the sum of vertically integrated water vapor, cloud, and rain (Fig. C1). A tile size of $16 \times 16 \text{ km}^2$ is chosen for this study as it represents the horizontal variability of moist patches associated with flower shallow cumuli in the simulations.

The partitioning of total water mixing ratio (q_t) is given by:

$$q_t = \overline{q_t} + q_t'' + q_t''' \quad . \quad (1)$$

The overline is the domain-mean, the double prime is the perturbation coarse-grained to $16 \times 16 \text{ km}^2$ tiles, representing variability associated with the mesoscale ($\geq 16 \text{ km}$). The triple prime represents variability associated with cumulus-scale processes ($< 16 \text{ km}$). The partitioning is detailed in Appendix D1.

The coarse-grained outputs are sorted by TWP and binned into quartiles. Quartile 1 (Q1) represents the driest and cloud-free areas while Quartile 4 (Q4) represents the moistest and cloudiest areas of the simulation. The $16 \times 16 \text{ km}^2$ tiles in each quartile are not necessarily adjacent to one another.

3.2 Shallow Convection Organization

Figure 3 shows the time series of the simulations. The thick solid lines represent the results from CTL. Sea surface temperature (SST) increases as the trajectory moves southwestward, and remains constant as the trajectory moves westward. The deepening of the cloud layer in CTL occurs after 6 UTC and becomes more obvious after 10 UTC, when the domain-mean vertical velocity (\overline{w}) shifts from negative to positive, helping the cloud layer to deepen (Fig 3b). After 20 UTC, the cloud depth remains constant as the boundary layer encounters large-scale subsidence.

The domain-mean TWP increases as the cloud layer deepens during the transition (Fig. 3d and Fig. C1). As the organization strengthens after 12 UTC, the TWP distribution becomes more asymmetrical; the moist areas become moister while the dry areas become drier (Fig. 3e). The variance of TWP normalized by the mean can be used as a proxy for the organization strength (Fig. 3f). The full 100-m resolution variance (black)

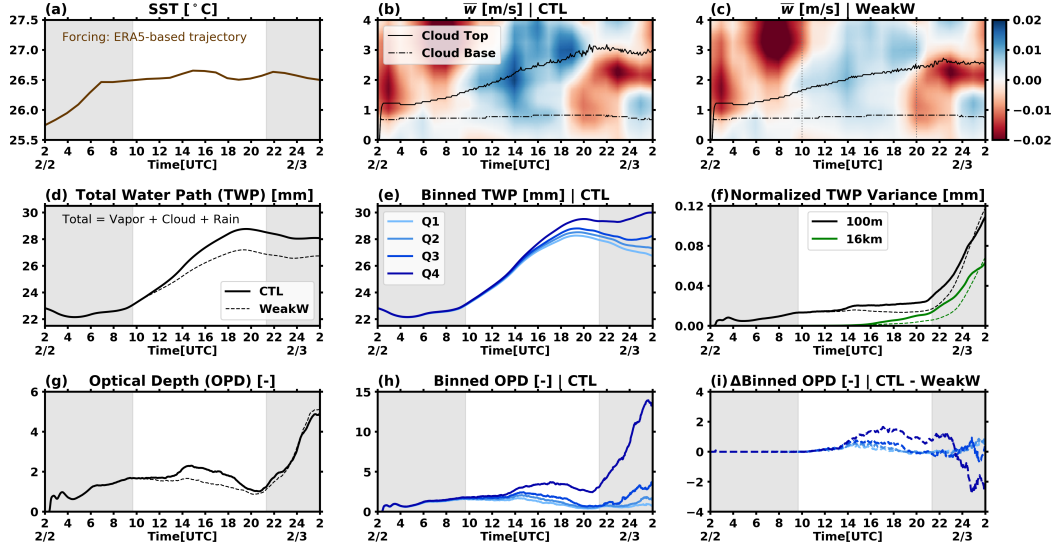


Figure 3. Time series of: (a) domain-mean sea surface temperature; (b) domain-mean vertical velocity, and cloud top and base heights, from CTL; (c) as in Panel (b) but for WeakW; (d) domain-mean total water path (TWP) of both CTL (solid) and WeakW (dash); (e) TWP sorted into quartiles from CTL; (f) variances of TWP computed at the full resolution (black) and the 16 km coarse-grained resolution (green), from both CTL (solid) and WeakW (dash); (g) domain-mean optical depth (OPD) from both simulations; (h) OPD from CTL binned by TWP into quartiles; (i) the change in OPD, binned by TWP, between CTL and WeakW. Gray shading is applied between the daylight hours of 5:48 am and 17:23 pm (local time), when the top-of-atmosphere incoming shortwave radiation exceeds zero in SAM.

235 increases first at 12 UTC, followed by the coarse-grained variance (green) which increases
 236 around 16 UTC; both of them increase rapidly after 22 UTC. This indicates that the or-
 237 ganized moist patches first strengthen gradually, and later the organization accelerates.
 238 During the transition, the total optical depth (OPD) increases, except for a dip around
 239 20 UTC (Fig. 3g-h), when the small isolated sugar clouds disappear while the larger cloud
 240 clusters have yet to aggregate and grow (Fig. 2h). After 20 UTC, the OPD also increases
 241 rapidly as the organization strengthens further. The first cold pool is observed at 22 UTC
 242 (Movie S2). Because the shallow cumuli in CTL do not precipitate until 20 UTC (Fig.
 243 C1c), approximately 4 hours after the mesoscale organization starts to take place, pre-
 244 cipitation is not essential for organization in the considered case. This finding is consis-
 245 tent with BB2017, but different from Seifert and Heus (2013) who found that cold pool
 246 formation is a dominant mechanism leading to cloud cluster formation.

247 Figure 4 shows the vertical profiles at two different times, during and after the sugar-
 248 to-flowers transition. At 16 UTC on February 2, the domain-mean cloud fraction (\overline{CF})
 249 and cloud fraction binned by TWP quartiles ($[CF]$) are bottom-heavy, with slightly en-
 250 hanced cloudiness near the cloud top in Q4. The enhanced cloudiness near cloud top in-
 251 dicates that the clouds begin to transition from the sugar state to the flower state. At
 252 2 UTC on February 3, the profiles become top-heavy, showing stratiform cloudiness, which
 253 is a distinct feature of the flower clouds (Bony et al., 2020; Rasp et al., 2020; Stevens et
 254 al., 2020). The stratiform cloudiness near the shallow cumulus cloud top is associated
 255 with pronounced longwave radiative cooling (Fig. C2a,c), consistent with previous stud-
 256 ies (Vogel et al., 2020).

257 At both times, regardless of the cloud states and the large-scale vertical velocity
 258 (\overline{w}), the binned mesoscale vertical velocity perturbations (w'') are positive in the cloud
 259 and subcloud layers and negative in the inversion layer of the moistest quartile (Q4). In
 260 the drier quartiles (Q1-Q2), the signs of w'' are opposite. The moist quartiles also have
 261 positive mesoscale total water perturbations (q_t''). These mesoscale perturbation profiles
 262 exhibit similar behaviors to those in BB2017, except with larger magnitudes at 2 UTC.
 263 Figure C2b,d further shows that the longwave radiative heating perturbations (R_{LW}'')
 264 are negative (more cooling) in the inversion layer of the moistest quartile where q_t'' is also
 265 positive and large, and positive (more heating) in the cloud and subcloud layer. This sug-
 266 gests that longwave radiation generates relatively more buoyant air in the cloud plume
 267 and less buoyant air in the inversion aloft, contributing to the mesoscale circulation be-

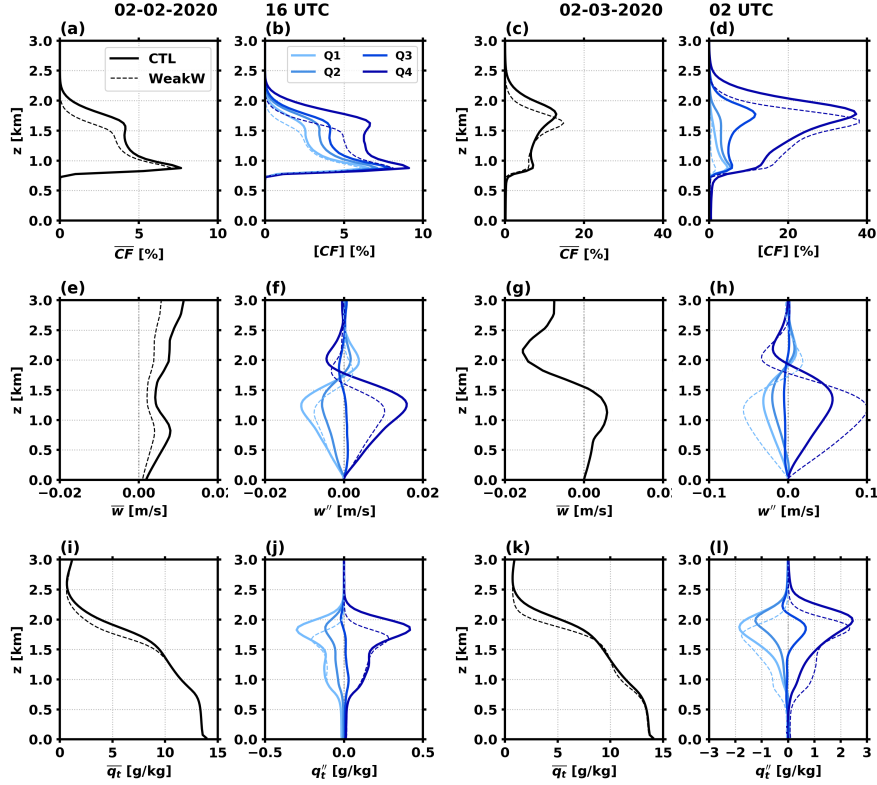


Figure 4. Vertical profiles of various variables at 16 UTC on February 2 (two left columns) and 2 UTC on February 3 (two right columns) of both CTL (solid) and WeakW (dash): (a,c) domain-mean cloud fraction (\overline{CF}); (b,d) cloud fraction binned by TWP quartiles ($[CF]$); (e,g) vertical velocity (\overline{w}); (f,h) mesoscale perturbations of vertical velocity binned by TWP quartiles (w''); (i,k) domain-mean total water mixing ratio ($\overline{q_t}$); and (j,l) mesoscale perturbations of total water (q_t''), binned by TWP quartiles. For the binned profiles, only Q1 and Q4 from WeakW are shown.

268 tween the moist and dry regions. During the daytime, the longwave radiation is almost
 269 balanced by the shortwave radiation (Fig. C2e-f), resulting in a negligible radiative con-
 270 tribution in the boundary layer, similar to BB2017. In the moist regions, there is also
 271 more latent heating in the subcloud and cloud layers due to more condensation, and more
 272 evaporative cooling in the inversion layer (Fig. C2j,l), which also contributes to w'' , con-
 273 sistent with BB2017.

274 Mass continuity requires that in the moist and cloudy regions, where w'' is posi-
 275 tive (negative) in the subcloud (inversion) layer, there is a local convergence (divergence)
 276 below (aloft) (see also BB2017). The profiles at both times have the same signs, but larger
 277 magnitudes at 2 UTC on February 3. This is because the cloud clusters are larger at the
 278 later time; therefore, coarse-graining does not wash out the variability associated with
 279 larger cloud clusters. Although cold pools are observed at the later time, at this stage of
 280 cold pool development, there is no significant difference in the dynamics (w'') compared
 281 to the stage prior to their formation. The same underlying mechanism associated with
 282 the mesoscale circulation still dominates. The following section will show that this lo-
 283 cal circulation is key to redistributing the total water, leading to mesoscale organization.

284 **4 The Mechanism of Transition**

285 This section analyzes the budget of mesoscale total water perturbations q_t'' in the
 286 four TWP quartiles to determine a mechanism responsible for the transition. In each TWP
 287 quartile, the mesoscale tiles are not necessarily adjacent to one another and they can change
 288 location in time based on the mesoscale TWP. Based on Equation 12 of BB2017 and the
 289 derivation in Appendix D, the budget of q_t'' at each level can be written as:

$$290 \quad \frac{\partial q_t''}{\partial t} = A + B + C + S_q'' \quad . \quad (2)$$

291 Each term on the right hand side of Equation (2) is described as follows: The first term
 292 is the advection of mesoscale variability due to trajectory-relative large-scale wind ($\bar{\mathbf{v}}$)
 293 and mesoscale perturbations of the wind velocity (\mathbf{v}''):

$$294 \quad A = -(\bar{\mathbf{v}} + \mathbf{v}'') \cdot \nabla q_t'' \quad . \quad (3)$$

295 Let $[\]$ denote coarse-graining of the cumulus-scale field inside the brackets to a mesoscale
 296 region of $16 \times 16 \text{ km}^2$, and let ρ denote the reference density profile. The second term rep-
 297 represents the vertical and horizontal gradients of the cumulus-scale q_t flux coarse-grained

298 to $16 \times 16 \text{ km}^2$:

$$299 \quad B = B_v + B_h = -\frac{1}{\rho} \frac{\partial}{\partial z} [\rho w''' q_t'''] - \nabla_h \cdot [\mathbf{v}''' q_t'''] \quad . \quad (4)$$

300 Eq. (4) was derived with the anelastic approximation used in SAM. The third term is
301 the mesoscale vertical advection of large-scale q_t :

$$302 \quad C = -w'' \frac{\partial \bar{q}_t}{\partial z} \quad . \quad (5)$$

303 Finally, the fourth term is the source term of q_t'' , which represents the mesoscale pertur-
304 bations of the precipitation mass flux (F_p) divergence:

$$305 \quad S_q'' = \left(-\frac{1}{\rho} \frac{\partial F_p}{\partial z}\right)'' \quad . \quad (6)$$

306 Figure 5(a-h) shows vertical profiles of A , B_v , B_h , and C binned by TWP quar-
307 tiles from CTL at 16 UTC on February 2 (two left columns) and 2 UTC on February
308 3 (two right columns). In each panel, the vertically integrated value of the respective quan-
309 tity between 0 and 3 km (denoted by $\langle \rangle$) is also shown. (The S_q'' profiles and their ver-
310 tically integrated values are much smaller and hence negligible even at 2 UTC on Febru-
311 ary 3, when the clouds precipitate, as shown in Figure C3a.) A positive quantity means
312 the respective term is responsible for moistening the region, a source term for q_t'' .

313 According to BB2017, A is small and tends to dry out the boundary layer in Q4.
314 Although this is true at 16 UTC on February 2 (Fig. 5a), A has a non-negligible mag-
315 nitude in the cloud layer at 2 UTC on February 3 (Fig. 5c). Nonetheless, $\langle A \rangle$ still dries
316 out Q4, and A is not a major term in the q_t'' budget.

317 Although B_v is large at both times, $\langle B_v \rangle$ is negligible in all quartiles. This is ex-
318 pected because the vertical cumulus-scale flux transfers total water vertically from the
319 cloud layer to the inversion layer but not horizontally. When coarse-grained within 16×16
320 km^2 regions, B_h is small and negligible at 16 UTC on February 2, but $\langle B_h \rangle$ is non-negligible
321 at 2 UTC on February 3 and contributes to drying in Q4, albeit secondary to $\langle A \rangle$.

322 At both times, the magnitude of C is larger than that of A and B_h , and $\langle C \rangle$ is the
323 only term that moistens the boundary layer in Q4, in which flower clouds aggregate. Be-
324 cause $\frac{\partial \bar{q}_t}{\partial z}$ is always negative (Fig. 4i,k), the sign of C always follows the sign of w'' . Due
325 to mass continuity, a positive C in the cloud layer of Q4 is associated with horizontal
326 total water convergence below the cloud plumes, and divergence in the inversion. A pos-
327 itive $\langle C \rangle$ indicates a net total water convergence in the lower troposphere of the moistest
328 quartile.

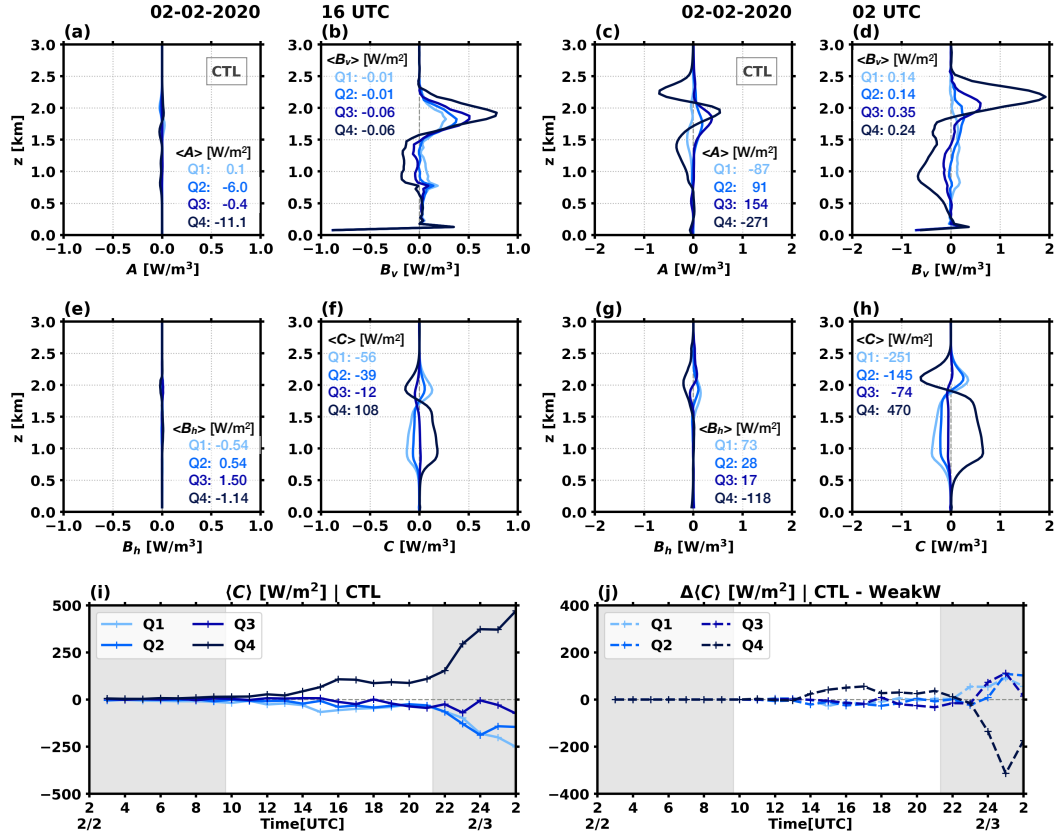


Figure 5. Vertical profiles of: (a,c) large-scale and mesoscale advection of q_t'' (A); (b,d) vertical gradient of the cumulus-scale vertical q_t flux (B_v); (e,g) horizontal gradient of the cumulus-scale horizontal q_t flux (B_h); and (f,h) mesoscale vertical advection of the large-scale q_t (C), at 16 UTC on February 2 (two left columns) and 2 UTC on February 3 (two right columns) from CTL, all coarse-grained to 16×16 km² tiles and binned by TWP. The vertically integrated values between 0 and 3 km are also shown, denoted by $\langle \rangle$. (i) Hourly time series of $\langle C \rangle$ binned by TWP quartiles from CTL. (j) The change in $\langle C \rangle$ time series between CTL and WeakW.

329 To demonstrate that $\langle C \rangle$ drives moistening in Q4 and drying in Q1 through Q3,
 330 Figure 5(i) shows the hourly time series of $\langle C \rangle$ binned by TWP quartiles from CTL. This
 331 provides the evidence that the net convergence and divergence of total water due to mesoscale
 332 circulation renders the moist and cloudy patches moister, and the dry and cloud-free patches
 333 drier.

334 5 The Role of Large-Scale Upward Motion

335 To examine the role of large-scale vertical velocity for the sugar-to-flower transi-
 336 tion, an additional simulation is performed and analyzed. Simulation WeakW has a 50 %
 337 weaker \bar{w} during the period of strong upward motion, i.e., between 10 UTC and 20 UTC
 338 which is referred to as the intermediate state of the sugar-to-flower transition (Fig. 3c).
 339 WeakW produces a shallower cloud layer and lower TWP than CTL. Figure 2k-o and
 340 Movie S3 show the cloud field evolution in WeakW. Simulation CTL exhibits a more rapid
 341 transition from the sugar to the flower cloud state than WeakW. It has greater normal-
 342 ized TWP variance and optical depth, especially in Q4 where flowers aggregate (Fig. 3f,i).

343 Although mesoscale organization forms more rapidly in CTL compared to WeakW
 344 during the intermediate state of the sugar-to-flower transition, the same mechanisms take
 345 place in both simulations. Moist areas become moister and dry areas become drier. Fig-
 346 ure 4f,j shows that with stronger upward motion, the w'' and q_t'' profiles of CTL during
 347 the transition period have the same structure as those in WeakW, except with larger mag-
 348 nitudes. In other words, the stronger upward motion assists the aggregation of total wa-
 349 ter on the mesoscale, accelerating organization.

350 The final organization state in WeakW is stronger than CTL, despite a slower tran-
 351 sition and weaker organization during the intermediate state. After 23 UTC, when the
 352 organization in WeakW catches up with CTL, w'' becomes stronger in WeakW than in
 353 CTL (Fig. 4l). This is consistent with the change in $\langle C \rangle$, which is greater in Q4 of CTL
 354 compared to WeakW between 10 UTC and 23 UTC (Fig. 5j), and smaller thereafter.
 355 A possible explanation is that the cloud clusters in WeakW are initially smaller and thus
 356 barely precipitate, whereas in CTL the clouds precipitate sooner and more strongly, so
 357 more and larger cold pools form in CTL (Fig. 2i-j,n-o and Fig. C1c). Therefore, more
 358 but smaller flowers form at the end of WeakW, as opposed to fewer but larger flowers
 359 with cold pools at the end of CTL.

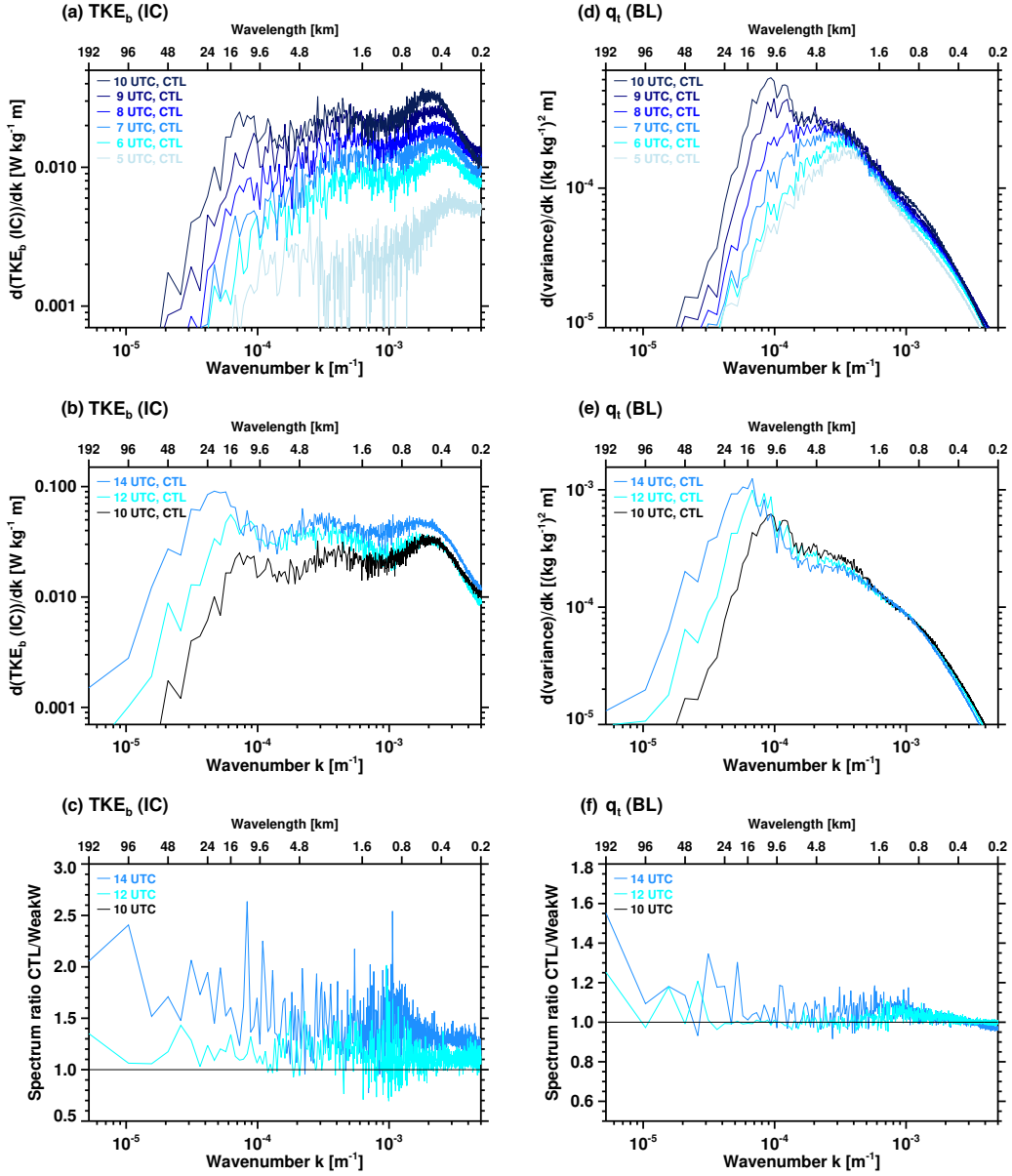


Figure 6. (a-b) Spectra of buoyant turbulence kinetic energy production in the cloud layer (TKE_b (IC)), expressed in units of W kg^{-1} of boundary-layer mass, plotted hourly from 5 UTC to 10 UTC and bi-hourly from 10 UTC to 14 UTC, respectively. (c) Ratio of the TKE_b (IC) spectra in CTL and WeakW plotted at 10, 12, and 14 UTC. (d-f) As in panels (a-c) but for total water mixing ratio in the boundary layer (q_t (BL)).

360 Figure 6 shows spectra of buoyant turbulence kinetic energy (TKE) production in
 361 the cloud layer (TKE_b (IC)) and of boundary-layer total water variance (q_t (BL)) de-
 362 rived from CTL, as well as the ratios of the spectra in CTL and WeakW. Circulation on
 363 the mesoscale and aggregation of moisture emerge in the form of peaks between 9.6 and
 364 16 km that are clearly discernible by 10 UTC (Fig. 6a,d) and continue to grow upscale
 365 as the clouds transition to the flower state (Fig. 6b,e). Up to 10 UTC, CTL and WeakW
 366 have the same \bar{w} , hence the spectra are identical and the ratios of TKE_b (IC) and q_t (BL)
 367 spectra are 1 (Fig. 6c,f).

368 In the following hours, the ratio of TKE_b (IC) spectra increases (Fig. 6c), suggest-
 369 ing that the stronger large-scale upward motion renders TKE production stronger in CTL
 370 compared to WeakW. The subcloud layer, on the other hand, consumes TKE produc-
 371 tion at specific mesoscale wavelengths (see Appendix C and Fig. C4). This indicates that
 372 the mesoscale circulation that emerges in the sugar-to-flower transition is predominantly
 373 driven by TKE production in the cloud layer. Finally, the ratio in the q_t (BL) spectra
 374 remains noisy at 12 UTC and increases at 14 UTC (Fig. 6f), albeit at a smaller mag-
 375 nitude than the TKE_b (IC) spectra. This is evidence that stronger large-scale upward
 376 vertical motion strengthens both the mesoscale TKE production and the moisture ag-
 377 gregation, the former more than the latter.

378 Figure 7 shows the ratio of integrated TKE_b (IC) and q_t (BL) spectra in CTL and
 379 WeakW. The spectra are integrated at three different wavelength bands, 0-4.8 km, 4.8-
 380 16 km, and 16-48 km. From the moment the two simulations diverge, i.e., 10 UTC, the
 381 ratio of the TKE production at the mesoscale (4.8-16 km and 16-48 km) exceeds the ra-
 382 tio of the TKE production at the smaller scale (0-4.8 km). This disproportionate strength-
 383 ening of cloud-level mesoscale TKE production relative to other scales, due to the more
 384 positive \bar{w} in CTL compared to WeakW, increases and persists over the period during
 385 which \bar{w} differs between the simulations. Additionally, the increase in the ratio of the
 386 TKE production leads a corresponding increase in the ratio of the QT variance delayed
 387 by approximately three hours, which indicates a causal relationship between the TKE
 388 production and the redistribution of the moisture. Therefore, it is the strengthening of
 389 cloud-level mesoscale TKE production in CTL relative to WeakW that strengthens ag-
 390 gregation of moisture on the mesoscale and accelerates the sugar-to-flower transition in
 391 response to a more positive \bar{w} .

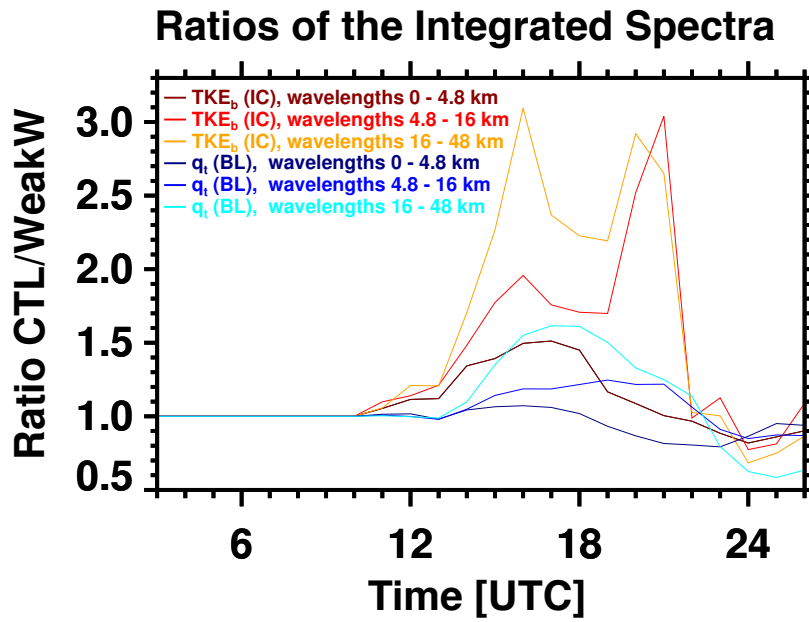


Figure 7. Time series of the ratio of integrated TKE_b (IC) spectra (warm colors) and the ratio of integrated q_t (BL) spectra. The ratio is between simulations CTL and WeakW. The spectra are integrated at three different wavelength bands: 0-4.8 km (small-scale), 4.8-16 km (meso- γ -scale), and 16-48 km (meso- β -scale).

392 **6 Conclusions**

393 The ATOMIC and EUREC⁴A field campaign took place in the Atlantic Ocean east
 394 of Barbados in January–February 2020, with a goal of better understanding the relation-
 395 ship between shallow cumuli and large-scale meteorological and oceanic conditions. On
 396 February 2–3, a transition of trade cumulus organization from sugar to flowers was ob-
 397 served. This study shows that a Lagrangian LES following a boundary-layer airmass tra-
 398 jectory can reproduce the transition. During the sugar-to-flowers transition, the clouds
 399 become organized, and the cloud layer deepens and moistens.

400 Although the large-scale vertical motion helps deepen the cloud layer, the mesoscale
 401 wind drives the sugar-to-flowers transition. The mesoscale circulation, driven by local
 402 ascending (descending) air inside (above) the shallow cumulus plumes, leads to a net mois-
 403 ture convergence in the moist patches, in which the clouds aggregate. This renders the
 404 moist patches moister and dry patches drier.

405 It is shown that large-scale vertical velocity regulates the sugar-to-flower transi-
 406 tion by modulating cloud-layer buoyant TKE production at the mesoscale, and the mesoscale
 407 circulation by which moisture aggregates. In the considered case, stronger large-scale up-
 408 ward motion accelerates the sugar-to-flower transition by strengthening cloud-layer mesoscale
 409 TKE production.

410 Given the broad interest in the vertical structure of subsidence engendered by ATOMIC
 411 and EUREC⁴A, a follow-on study examining how the structure of the large-scale ver-
 412 tical velocity impacts the mesoscale organization is warranted. Because of the presence
 413 of mineral dust, a follow-on study examining the sensitivity of the shallow cumulus or-
 414 ganization to mineral dust will be conducted. Precipitation and cold pools may also af-
 415 fect the rate of mesoscale organization and the cloud cluster sizes; hence, a future study
 416 will also explore these relationships.

417 **Appendix A The Initialization of Sea Salt and Mineral Dust**

418 Sea salt and mineral dust are initialized at the beginning of both the CTL and WeakW
 419 simulations (see Section 2.2 and Fig. A1). The details on the initialization are as follows.

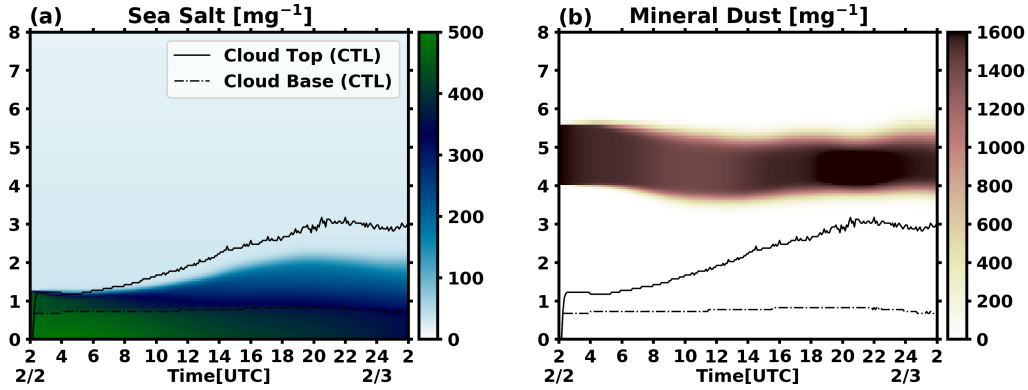


Figure A1. Time series of the domain-mean (a) sea salt and (b) mineral dust concentration from CTL. In both panels, the solid and dash-dot lines indicate the cloud-top and cloud-base heights of the simulation.

A1 Sea-Salt Particles

The sea-salt particles in the boundary layer are initialized based on in-situ aerosol data measured from the RHB averaged between 0 UTC and 4 UTC on February 2. The aerosol size distribution is bimodal and fitted with lognormal functions (Fig. A2). The first peak has a geometric mean diameter (D_g) and geometric standard deviation (σ_g) of $0.128 \mu\text{m}$ and 1.71 , respectively, and the initial concentration (N) is 400 mg^{-1} . The second peak's D_g and σ_g are $0.961 \mu\text{m}$ and 1.73 , respectively, and N is 13 mg^{-1} . The sea-salt particles in the free troposphere have initial N of 32 mg^{-1} , consistent with the EUREC⁴A measurements from the Ultra-High-Sensitivity Aerosol Spectrometer (UH-SAS) and the Cloud Droplet Probe (CDP-2) on the French ATR-42 research aircraft (personal communication with Pierre Coutris, September 30, 2020). The sea salt is coupled with the cloud microphysics scheme.

A2 Mineral Dust

Mineral dust was present in an elevated layer east of Barbados between January 31 and February 3. Therefore, a mineral dust layer is placed in the simulation between 4 and 5.5 km, colocated with an elevated moist layer, based on a previous study which showed that the long-ranged transported Saharan air layer carries mineral dust and moisture from Africa to the Caribbean (Gutleben et al., 2019). The initial mineral dust concentration inside the layer is $1,600 \text{ mg}^{-1}$. Dust optical properties are calculated based

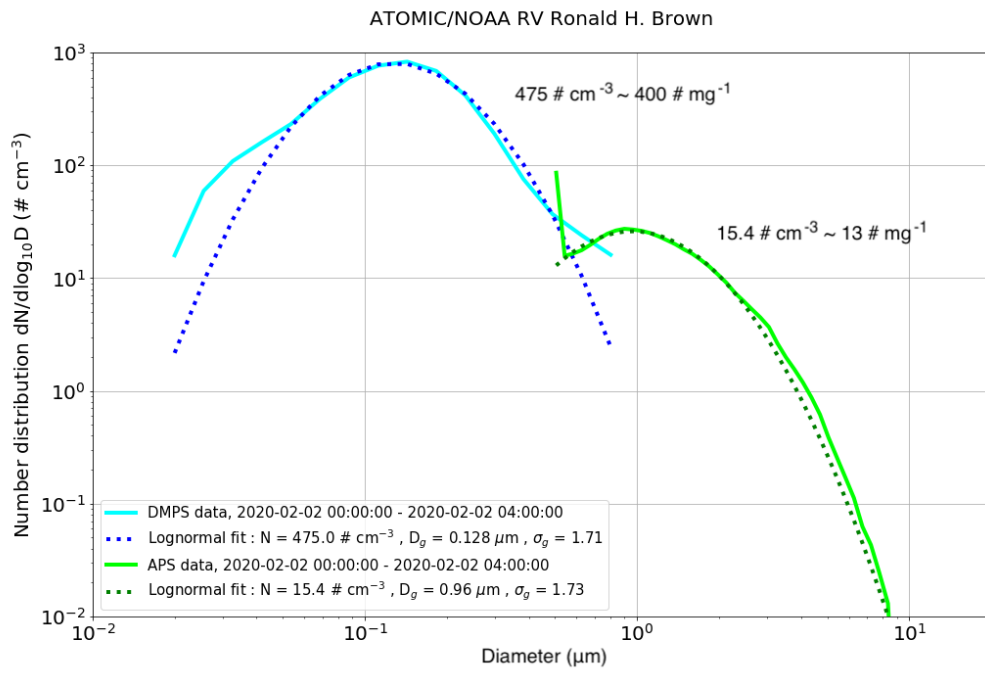


Figure A2. Aerosol size distribution (solid lines) measured from the RHB, averaged between 0 UTC and 4 UTC on February 2, 2020, used to initialize sea-salt aerosol in the simulations. The aerosol size distribution is bimodal and fitted with lognormal functions (dotted lines).

439 on the assumed size distribution and refractive indices in d’Almeida et al. (1991). The
 440 single scattering albedo is approximately 0.85. As a result, the aerosol optical depth of
 441 the mineral dust is approximately 0.35, consistent with the MODIS observation during
 442 the period of interest. The mineral dust is coupled with the radiation scheme, but not
 443 with the cloud microphysics, as the dust remains in the free troposphere in this simu-
 444 lation.

445 To confirm that the mineral dust configuration described above is consistent with
 446 the observation, two additional Eulerian simulations are performed. Figure A3 shows that
 447 the clear-sky surface radiations in SAM are more consistent with the in-situ measure-
 448 ments when the mineral dust is included. Since the RHB was stationary between Febru-
 449 ary 1-2, during which there is a cloud-free period, the additional simulations’ domain is
 450 fixed at the RHB location. The forcings are driven with ERA5, similar to the Lagrangian
 451 simulations presented in the main manuscript, except the large-scale horizontal advec-
 452 tion tendency of the temperature and humidity is included. These additional simulations
 453 are configured with 50 m horizontal grid spacing and a horizontal domain extent of 40×40
 454 km^2 . The vertical grid spacing, domain top height, and cloud microphysics and radia-
 455 tion schemes of these Eulerian simulations are the same as those of the Lagrangian sim-
 456 ulations. During the cloud-free period, the implemented mineral dust layer increases the
 457 surface downward shortwave radiation by approximately 70 W/m^2 , making it more con-
 458 sistent with the observation from the RHB. The contribution of the mineral-dust layer
 459 on the surface longwave radiation is small, albeit in the right direction.

460 **Appendix B Determining the Tile Size for Coarse-Graining**

461 The ratio of total water path variance is used to determine the tile size for coarse-
 462 graining. The ratio is between TWP coarse-grained to different tile sizes ($\text{Var}(\text{TWP})_{\text{Tile}}$)
 463 and TWP at the full 100 m resolution ($\text{Var}(\text{TWP})_{100\text{m}}$), and is referred to as the ‘TWP
 464 variance ratio’ for short. (See Honnert et al. (2011) for examples of this approach be-
 465 ing applied to other variables.) Figure B1 shows the TWP variance ratio from 4 UTC
 466 on February 2, 2020 to 2 UTC on February 3, 2020, plotted every 2 hours from CTL.
 467 The tile sizes are multiples of the horizontal grid spacing, from 200 m to 64 km. The TWP
 468 variance ratio is 1 if the tile size is 100 m (the horizontal grid spacing), and reduces to
 469 smaller values as the tile sizes become larger. When the TWP variance ratio is below
 470 the e -folding value (horizontal gray line), the tile size is too coarse to represent the vari-

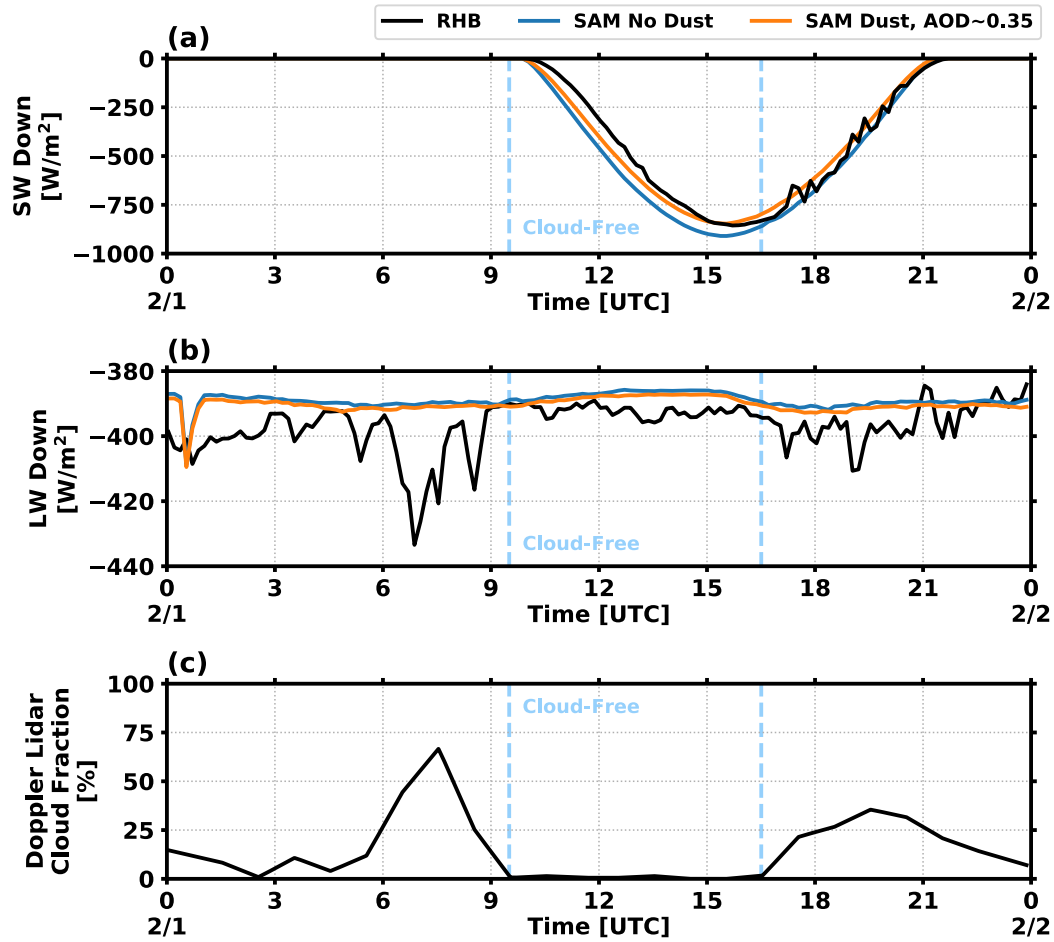


Figure A3. (a) A comparison of the downward shortwave radiation from the RHB in-situ measurement (black) and the Eulerian simulations with mineral dust (orange) and without mineral dust (blue). (b) As in panel (a) but for the downward longwave radiation. (c) Time series of the cloud fraction measured by the Doppler lidar at the RHB.

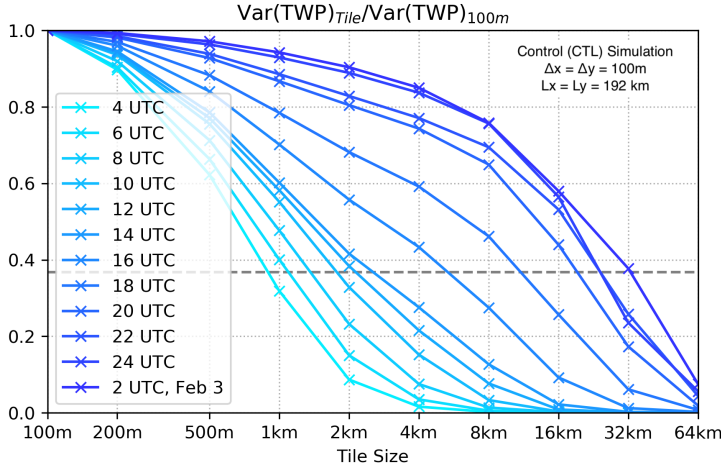


Figure B1. The TWP variance ratio, or the ratio of the variance of total water path coarse-grained to different tile sizes ($\text{Var}(\text{TWP})_{\text{Tile}}$) to the variance of 100-m resolution total water path ($\text{Var}(\text{TWP})_{100\text{m}}$), computed at different tile sizes from 200 m to 64 km for CTL. The horizontal gray dash line indicates the e -folding value. See text in Section 2 above for details.

471 ability of TWP within the domain on the scale represented by the tile. Since the mesoscale
 472 organization strengthens rapidly after 20 UTC, as measured by the normalized TWP vari-
 473 ance (Fig. 3f), we look for the tile sizes that can still represent the variability of TWP
 474 within the domain after that time. The TWP variance ratio from CTL is above the e -
 475 folding value between 20 UTC on February 2 and 2 UTC on February 3 for the tile size
 476 of 16 km. Therefore, we pick 16 km as the tile size for coarse-graining in CTL.

477 Appendix C Additional Figures

478 This section provides additional figures for the discussion in Sections 3 through 5
 479 of the main manuscript.

480 Figure C1 shows the time series of the vertically integrated water vapor, cloud wa-
 481 ter, and rain water, also known as precipitable water, cloud water path, and rain water
 482 path. The time series are from simulations CTL and WeakW. The sum of these quan-
 483 tities equals the total water path (Fig. 3d).

484 Figure C2 shows the vertical profiles from simulation CTL: (top) longwave radiative
 485 heating rate, (center) shortwave radiative heating rate, and (bottom) latent heat-

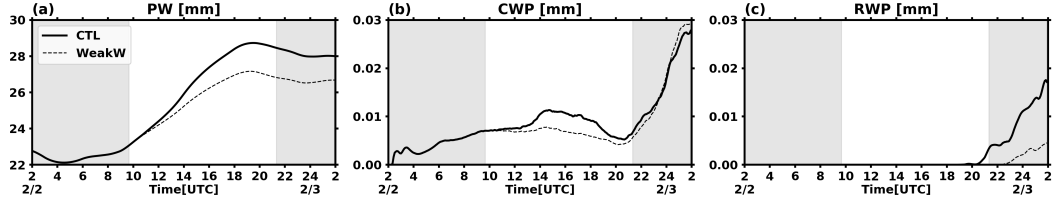


Figure C1. Time series of domain-mean: (a) water vapor path or precipitable water, (b) cloud water path, and (c), rain water path from CTL and WeakW. The sum of these three quantities are total water path, shown in Figure 3d in the main manuscript.

486 ing rate associated with net evaporation and condensation. See Section 3.2 and figure
 487 caption for details.

488 Figure C3 shows the vertical profiles from simulation CTL of the mesoscale per-
 489 turbations of the precipitation mass flux divergence at 2 UTC on February 3, and the
 490 central difference of the mesoscale total water mixing ratio perturbations about 2 UTC.
 491 Since the 3D outputs are saved every 15 minutes, $\Delta t = 30 \text{ min}$ and $\langle \frac{\Delta q_t''}{\Delta t} |_{30min} \rangle$ does
 492 not necessarily equal the sum of the right hand side of Equation (2) in the main manuscript
 493 because of the large time interval. But the approximation

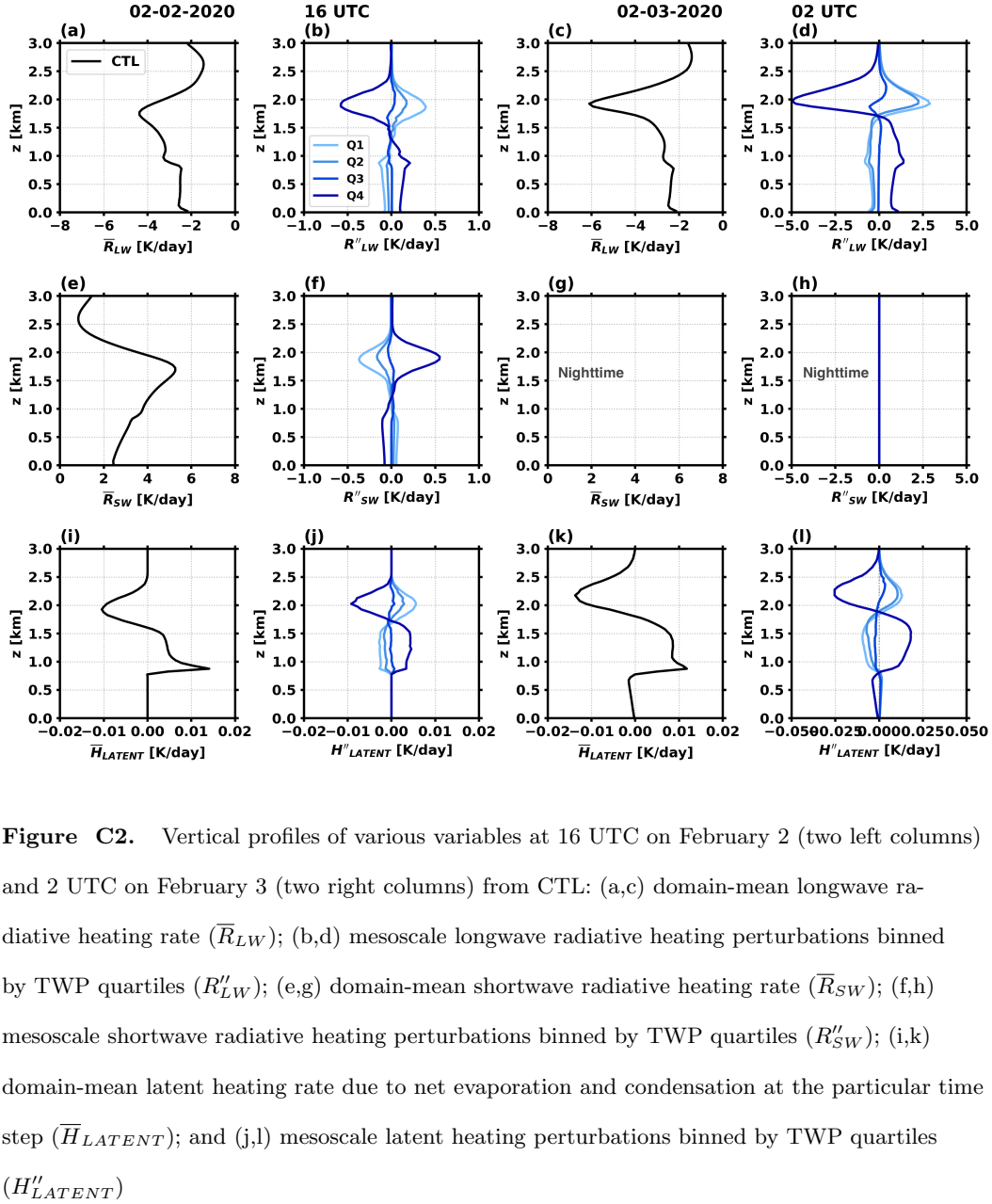
$$\langle \frac{\Delta q_t''}{\Delta t} |_{30min} \rangle \approx \langle A \rangle + \langle B_v \rangle + \langle B_h \rangle + \langle C \rangle + \langle S_q'' \rangle$$

494 still holds, and the moister quartiles get moister and the drier quartiles get drier.

495 Figure C4 shows the spectra of buoyant TKE production in the subcloud layer (TKE_b
 496 (SC)). The spectra are expressed in the unit of W kg^{-1} of boundary layer mass, enabling
 497 a comparison of the spectra in the subcloud layer with the cloud layer (Fig. 6a-b) not
 498 only in terms of shape, but also magnitude. After 10 UTC, the TKE_b (SC) spectra de-
 499 crease with time and is negative at the mesoscale (approximately 9.6-24 km wavelength).
 500 The negative spectra do not appear on the logarithmic axis. This indicates that the sub-
 501 cloud layer consumes TKE at specific mesoscale wavelengths. It is the TKE production
 502 in the cloud layer that drives the mesoscale circulation which emerges in the sugar-to-
 503 flower transition.

504 Appendix D Mesoscale Tracer Budget Derivation

505 This section explains the derivation of the budget of a tracer on a (mesoscale) re-
 506 gion in detail. The derivation in Section D3 makes no assumptions simplifying the Navier-



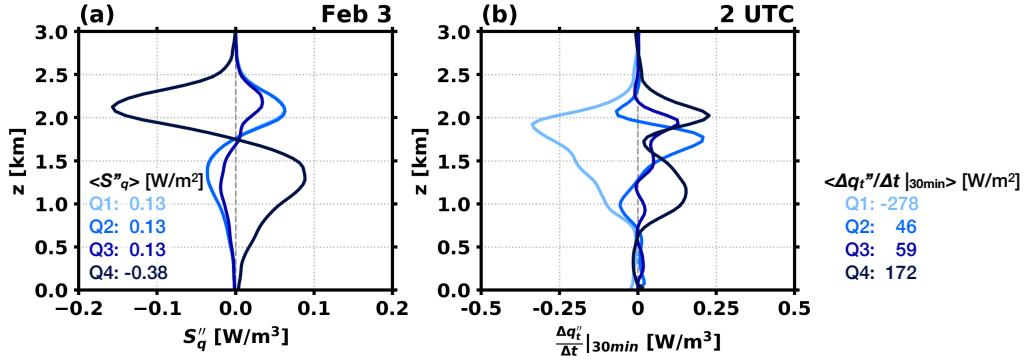


Figure C3. Vertical profiles of (a) mesoscale perturbations of the precipitation flux divergence binned by TWP quartiles at 2 UTC on February 3, and (b) central difference of the mesoscale total water mixing ratio perturbations (q''_t) about 2 UTC.

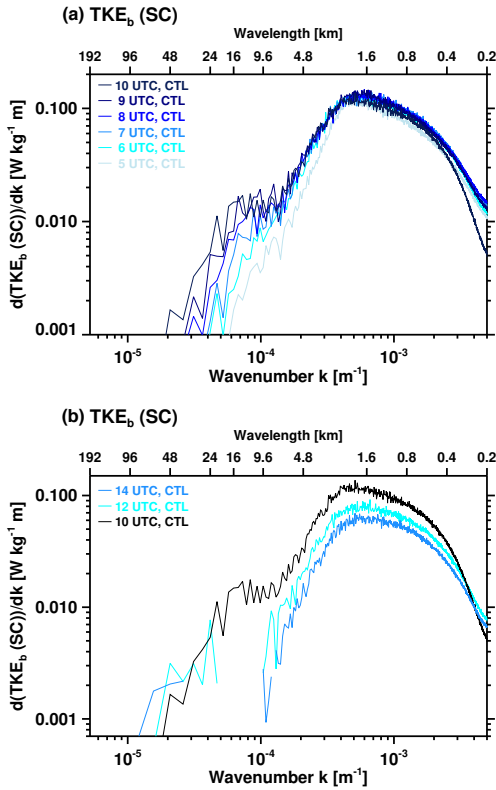


Figure C4. Spectra of buoyant turbulence kinetic energy production in the subcloud layer (TKE_b (SC)), plotted (a) hourly from 5 UTC to 10 UTC and (b) bi-hourly from 10 UTC to 14 UTC.

507 Stokes equations. The anelastic approximation and a scale-separation approximation are
 508 applied in Section D4 to obtain the budget of a tracer on a (mesoscale) region derived
 509 by BB2017.

510 **D1 Definitions**

511 Let f be a function that is defined on the locations x_i, y_j, z_k and times t_l of the sim-
 512 ulation domain

$$f \doteq f(x_i, y_j, z_k, t_l) \quad . \quad (\text{D1})$$

513 Decompose f into its domain horizontal mean \bar{f} and the local deviation f' from this mean:

$$f \doteq \bar{f} + f' \quad (\text{D2})$$

514 Now consider a horizontal, rectangular (mesoscale) region covering $m \times n$ locations in
 515 the x and y dimensions, and let the square brackets $[\]$ denote the horizontal mean over
 516 the region:

$$[f] \doteq \frac{1}{mn} \sum_{m,n} f(x_i, y_j, z_k, t_l) \quad . \quad (\text{D3})$$

517 (See Section 2 in the SI for how the size of the region is determined for the simulation
 518 presented in the manuscript.) We decompose f into

$$f \doteq \bar{f} + f'' + f''' \quad . \quad (\text{D4})$$

519 f'' is the deviation of the region mean from the domain mean,

$$f'' \doteq [f] - \bar{f} \quad , \quad (\text{D5})$$

520 and f''' the local deviation from the region mean:

$$f''' \doteq f - [f] \quad . \quad (\text{D6})$$

521 **D2 Identities**

522 The following identities are used in the derivation of the mesoscale tracer budget.

523 Firstly,

$$f' = f'' + f''' \quad . \quad (\text{D7})$$

524 Since $[f]$ is constant over the region, we find

$$[[f]] = [f] \quad . \quad (\text{D8})$$

525 Applying the horizontal mean over the region [] to (D6) gives

$$[f'''] = 0 \quad . \quad (D9)$$

526 The relationships

$$[f'] = [f''] \quad , \quad (D10)$$

527

$$[f'''] = f'' \quad , \quad (D11)$$

528

$$f'' = [f'] \quad . \quad (D12)$$

529 are elementary. Furthermore, we note that because \bar{f} and f'' are constant over the re-
530 gion, for a function $g \doteq g(x_i, y_j, z_k, t_l)$,

$$[\bar{f}g] = \bar{f}[g] \quad , \quad (D13)$$

531

$$[f''g] = f''[g] \quad , \quad (D14)$$

532 and

$$[\bar{f}g'''] = \bar{f}[g'''] = 0 \quad , \quad (D15)$$

533

$$[f''g'''] = f''[g'''] = 0 \quad . \quad (D16)$$

534 From the definition of the horizontal mean over the region [] we obtain

$$[\nabla f] = \nabla[f] \quad . \quad (D17)$$

535 The identities above hold for vectors in place of the scalars f or g . Then, because g'' and
536 therefore $\nabla g''$ are constant over the region,

$$[\mathbf{v}''' \cdot \nabla g''] = [\mathbf{v}'''] \cdot \nabla g'' = 0 \quad . \quad (D18)$$

537 Based on the definition (D6) and using (D17),

$$[\nabla f'''] = [\nabla f] - [\nabla[f]] = [\nabla f] - [[\nabla f]] = [\nabla f] - [\nabla f] = 0 \quad . \quad (D19)$$

538 We did not make use of the identity $[f'''] = 0$ (Eq. D9), because in general, $[g] = 0$
539 does not imply $[\nabla g] = 0$.

540 Because $\bar{\mathbf{v}}$ and \mathbf{v}'' are constant over the region, we obtain

$$[\bar{\mathbf{v}} \cdot \nabla f'''] = \bar{\mathbf{v}} \cdot [\nabla f'''] = 0 \quad , \quad (D20)$$

541

$$[\mathbf{v}'' \cdot \nabla f'''] = \mathbf{v}'' \cdot [\nabla f'''] = 0 \quad . \quad (D21)$$

542 **D3 Derivation of the mesoscale tracer budget**

543 The continuity equation for a scalar with the mixing ratio q is

$$\frac{\partial(q\rho)}{\partial t} = -\nabla \cdot \mathbf{F}_q + \tilde{S}_q \quad , \quad (\text{D22})$$

544 where ρ is the air mass density, and \mathbf{F}_q the flux and \tilde{S}_q the source of q , respectively. Us-
545 ing the mass continuity equation and the air velocity $\mathbf{v} = (u, v, w)$, it can be written
546 as

$$\frac{\partial q}{\partial t} = -\mathbf{v} \cdot \nabla q + S_q \quad , \quad (\text{D23})$$

547 where we set $S_q \doteq \tilde{S}_q/\rho$. Using the decomposition (D2) for q and S_q , so that

$$q = \bar{q} + q' \quad , \quad (\text{D24})$$

548 and

$$S_q = \bar{S}_q + S'_q \quad , \quad (\text{D25})$$

549 and noting that

$$\frac{\partial \bar{q}}{\partial t} = \bar{S}_q \quad , \quad (\text{D26})$$

550 we obtain

$$\frac{\partial q'}{\partial t} = -(\mathbf{v} \cdot \nabla q' + w' \frac{d\bar{q}}{dz}) + S'_q \quad . \quad (\text{D27})$$

551 Applying the horizontal mean over the region [] on both sides of (D27), and using the
552 identity (D12) produces

$$\frac{\partial q''}{\partial t} = -[\mathbf{v} \cdot \nabla q' + w' \frac{d\bar{q}}{dz}] + S''_q \quad , \quad (\text{D28})$$

553 which simplifies to

$$\frac{\partial q''}{\partial t} = -[\mathbf{v} \cdot \nabla q'] - w'' \frac{d\bar{q}}{dz} + S''_q \quad . \quad (\text{D29})$$

554 Expanding the first term on the right hand side gives:

$$[\mathbf{v} \cdot \nabla q'] = [(\bar{\mathbf{v}} + \mathbf{v}'' + \mathbf{v}''') \cdot \nabla (q'' + q''')] \quad , \quad (\text{D30})$$

$$= [(\bar{\mathbf{v}} + \mathbf{v}'') \cdot \nabla q''] + [\mathbf{v}''' \cdot \nabla q''] + [(\bar{\mathbf{v}} + \mathbf{v}'') \cdot \nabla q'''] + [\mathbf{v}''' \cdot \nabla q'''] \quad . (\text{D31})$$

555 With suitable identities, this simplifies to

$$[\mathbf{v} \cdot \nabla q'] = (\bar{\mathbf{v}} + \mathbf{v}'') \cdot \nabla q'' + [\mathbf{v}''' \cdot \nabla q'''] \quad . \quad (\text{D32})$$

556 Inserting (D43) into (D29) produces the budget of a tracer on a (mesoscale) region

$$\frac{\partial q''}{\partial t} = -(\bar{\mathbf{v}} + \mathbf{v}'') \cdot \nabla q'' - [\mathbf{v}''' \cdot \nabla q'''] - w'' \frac{d\bar{q}}{dz} + S''_q \quad . \quad (\text{D33})$$

557 On the right hand side, the first term is associated with advection of mesoscale variabil-
 558 ity. The second term represents sub-mesoscale processes, such as individual cumulus clouds.
 559 The third term is associated with mean mesoscale vertical advection of the large scale
 560 vertical tracer gradient. The last term, the tracer source, can represent non-advective
 561 transport, such as sedimentation. When the tracer q is total moisture, then

$$S_q'' = \left(-\frac{1}{\rho} \nabla \cdot \mathbf{F}_p\right)'' = \left(-\frac{1}{\rho} \frac{\partial F_p}{\partial z}\right)'' \quad , \quad (\text{D34})$$

562 is the precipitation flux divergence, with the precipitation flux $\mathbf{F}_p = (0, 0, F_p)$. As shown
 563 in Figures 5 and C3, for shallow cumuli that barely precipitate, the term S_q'' is much smaller
 564 than the other terms on the right hand side of Eq. (D33).

565 **D4 Anelastic approximation**

566 In the anelastic approximation of the Navier-Stokes equations,

$$\frac{\partial \rho}{\partial t} = \nabla \cdot (\rho \mathbf{v}) \doteq 0 \quad , \quad (\text{D35})$$

567 and

$$\frac{\partial \rho}{\partial x} \doteq \frac{\partial \rho}{\partial y} \doteq 0 \quad . \quad (\text{D36})$$

568 Then, for a scalar $f = f(x_i, y_j, z_k, t_l)$, we obtain from (D35)

$$\nabla \cdot (\rho \mathbf{v} f) = \rho \mathbf{v} \cdot \nabla f \quad . \quad (\text{D37})$$

569 This also holds for $f = q'''$:

$$\nabla \cdot (\rho \mathbf{v} q''') = \rho \mathbf{v} \cdot \nabla q''' \quad , \quad (\text{D38})$$

570 or, equivalently,

$$\mathbf{v} \cdot \nabla q''' = \frac{1}{\rho} \nabla \cdot (\rho \mathbf{v} q''') \quad . \quad (\text{D39})$$

571 Decomposing $\mathbf{v} = \bar{\mathbf{v}} + \mathbf{v}'' + \mathbf{v}'''$ and applying the horizontal mean over the region []

572 gives

$$[(\bar{\mathbf{v}} + \mathbf{v}'' + \mathbf{v}''') \cdot \nabla q'''] = \frac{1}{\rho} [\nabla \cdot (\rho (\bar{\mathbf{v}} + \mathbf{v}'' + \mathbf{v}''') q''')] \quad . \quad (\text{D40})$$

573 On the right hand side of (D40), the brackets [] commuted with $\frac{1}{\rho}$ because of (D36).

574 Using suitable identities, we obtain

$$[\mathbf{v}''' \cdot \nabla q'''] = \frac{1}{\rho} [\nabla \cdot (\rho \mathbf{v}''' q''')] \quad . \quad (\text{D41})$$

575 Inserting (D41) into (D33) yields the budget of a tracer on a (mesoscale) region in which
 576 the sub-mesoscale term was converted using the anelastic approximation:

$$\frac{\partial q''}{\partial t} = -(\bar{\mathbf{v}} + \mathbf{v}'') \cdot \nabla q'' - \frac{1}{\rho} [\nabla \cdot (\rho \mathbf{v}''' q''')] - w'' \frac{d\bar{q}}{dz} + S_q'' \quad . \quad (\text{D42})$$

577 Expanding the second term on the right hand side of (D42) with $\mathbf{v} = (u, v, w)$ gives

$$\frac{1}{\rho} [\nabla \cdot (\rho \mathbf{v}''' q''')] = \frac{\partial}{\partial x} [u''' q'''] + \frac{\partial}{\partial y} [v''' q'''] + \frac{1}{\rho} \frac{\partial}{\partial z} [\rho w''' q'''] \quad . \quad (\text{D43})$$

578 Using the scale separation approximation (BB2017, Eq. (28))

$$\nabla_h \cdot [\mathbf{v}''' q_t'''] = \frac{\partial}{\partial x} [u''' q_t'''] + \frac{\partial}{\partial y} [v''' q_t'''] \ll \frac{1}{\rho} \frac{\partial}{\partial z} [\rho w''' q_t'''] \quad (\text{D44})$$

579 gives

$$\frac{\partial q''}{\partial t} = -(\bar{\mathbf{v}} + \mathbf{v}'') \cdot \nabla q'' - \frac{1}{\rho} \frac{\partial}{\partial z} [\rho w''' q_t'''] - w'' \frac{d\bar{q}}{dz} + S_q'' \quad . \quad (\text{D45})$$

580 This is the budget of a tracer on a (mesoscale) region in the anelastic approximation de-
 581 rived by BB2017, in their Eq. (31).

582 In the main manuscript, the full budget of the mesoscale tracer (Eq. (D42)) prior
 583 to applying the scale separation approximation is used. This is because toward
 584 the end of the simulations, the scale separation approximation or Eq. (D44) does not
 585 hold true.

586 Therefore, Eq. (D42) can be written as:

$$\frac{\partial q''}{\partial t} = -(\bar{\mathbf{v}} + \mathbf{v}'') \cdot \nabla q'' - \frac{1}{\rho} \frac{\partial}{\partial z} [\rho w''' q_t'''] - \nabla_h \cdot [\mathbf{v}''' q_t'''] - w'' \frac{d\bar{q}}{dz} + S_q'' \quad , \quad (\text{D46})$$

587 which is consistent with Equations (2) - (6) in the main manuscript.

588 Acknowledgments

589 This study was supported by NOAA's Climate Program Office, Climate Variability and
 590 Predictability Program (GC19-303). This is PMEL contribution number: 5239. The au-
 591 thors thank scientists, technicians, pilots, crew members, and everybody who made the
 592 ATOMIC and EUREC⁴A field campaign possible. We thank Marat Khairoutdinov, Stony
 593 Brook University, for providing the System for Atmospheric Modeling (SAM). We thank
 594 Pierre Coutris, French National Centre for Scientific Research (CNRS), for providing data
 595 from the Ultra-High-Sensitivity Aerosol Spectrometer (UHSAS) and the Cloud Droplet
 596 Probe (CDP-2) on the French ATR-42 research aircraft. We thank Raphaela Vogel, LMD/IPSL,

597 CNRS, Sorbonne University, Paris, France, and two anonymous reviewers whose com-
 598 ments helped improve the manuscript. We acknowledge the NOAA Research and De-
 599 velopment High Performance Computing Program for providing computing and storage
 600 resources that have contributed to the research results reported within this paper. ERA5
 601 data were generated using Copernicus Climate Change Service Information. Neither the
 602 European Commission or ECMWF is responsible for any use that may be made of the
 603 Copernicus information or data in this publication. Simulation outputs from this study
 604 are available at [https://csl.noaa.gov/groups/cs19/datasets/data/cloud_phys/2021](https://csl.noaa.gov/groups/cs19/datasets/data/cloud_phys/2021-Narenpitak-etal/)
 605 [-Narenpitak-etal/](https://csl.noaa.gov/groups/cs19/datasets/data/cloud_phys/2021-Narenpitak-etal/).

606 References

- 607 Blossey, P. N., Bretherton, C. S., Zhang, M., Cheng, A., Endo, S., Heus, T., . . . Xu,
 608 K. M. (2013). Marine low cloud sensitivity to an idealized climate change: The
 609 CGILS LES intercomparison. *Journal of Advances in Modeling Earth Systems*,
 610 5(2), 234–258. doi: 10.1002/jame.20025
- 611 Bony, S., & Dufresne, J. L. (2005). Marine boundary layer clouds at the heart of
 612 tropical cloud feedback uncertainties in climate models. *Geophysical Research*
 613 *Letters*, 32(20), 1–4. doi: 10.1029/2005GL023851
- 614 Bony, S., Schulz, H., Vial, J., & Stevens, B. (2020). Sugar, gravel, fish, and flowers:
 615 Dependence of mesoscale patterns of trade-wind clouds on environmental con-
 616 ditions. *Geophysical Research Letters*, 47(7), 1–9. doi: 10.1029/2019gl085988
- 617 Boucher, O., Randall, D., Artaxo, P., Bretherton, C., Feingold, G., Forster, P.,
 618 . . . Zhang, X. Y. (2013). Clouds and aerosols. In *Climate change 2013*
 619 *the physical science basis: Working group i contribution to the fifth as-*
 620 *essment report of the intergovernmental panel on climate change.* doi:
 621 10.1017/CBO9781107415324.016
- 622 Bretherton, C. S., & Blossey, P. N. (2017). Understanding mesoscale aggregation of
 623 shallow cumulus convection using large-eddy simulation. *Journal of Advances*
 624 *in Modeling Earth Systems*, 9(8), 2798–2821. doi: 10.1002/2017MS000981
- 625 Bretherton, C. S., Blossey, P. N., & Jones, C. R. (2013). Mechanisms of marine low
 626 cloud sensitivity to idealized climate perturbations: A single-LES exploration
 627 extending the CGILS cases. *Journal of Advances in Modeling Earth Systems*,
 628 5(2), 316–337. doi: 10.1002/jame.20019

- 629 d’Almeida, G. A., Koepke, P., & Shettle, E. P. (1991). *Atmospheric aerosols: Global*
630 *climatology and radiative characteristics*. Hampton, Va.: A. Deepak Pub.
- 631 Feingold, G., Walko, R. L., Stevens, B., & Cotton, W. R. (1998). Simulations of ma-
632 rine stratocumulus using a new microphysical parameterization scheme. *Atmo-*
633 *spheric Research*, 47–48, 505–528. doi: 10.1016/S0169-8095(98)00058-1
- 634 Gutleben, M., Groß, S., Wirth, M., Emde, C., & Mayer, B. (2019). Impacts of Water
635 Vapor on Saharan Air Layer Radiative Heating. *Geophysical Research Letters*,
636 46(24), 14854–14862. doi: 10.1029/2019GL085344
- 637 Hersbach, H., Bell, B., Berrisford, P., Hirahara, S., Horányi, A., Muñoz-Sabater,
638 J., ... Thépaut, J.-N. (2020). The ERA5 global reanalysis. *Quarterly*
639 *Journal of the Royal Meteorological Society*, 146(730), 1999–2049. doi:
640 <https://doi.org/10.1002/qj.3803>
- 641 Holland, J. Z., & Rasmusson, E. M. (1973). Measurements of the atmospheric
642 mass, energy, and momentum budgets over a 500-kilometer square of trop-
643 ical ocean. *Monthly Weather Review*, 101(1), 44 - 55. doi: 10.1175/
644 1520-0493(1973)101<0044:MOTAME>2.3.CO;2
- 645 Honnert, R., Masson, V., & Couvreux, F. (2011). A diagnostic for evaluating the
646 representation of turbulence in atmospheric models at the kilometeric scale.
647 *Journal of the Atmospheric Sciences*, 68(12), 3112–3131.
- 648 Khairoutdinov, M. F., & Randall, D. A. (2003). Cloud Resolving Modeling of
649 the ARM Summer 1997 IOP: Model Formulation, Results, Uncertainties, and
650 Sensitivities. *Journal of the Atmospheric Sciences*, 60(4), 607–625. doi:
651 10.1175/1520-0469(2003)060<0607:CRMOTA>2.0.CO;2
- 652 Lamer, K., Kollias, P., & Nuijens, L. (2015). Observations of the variability of
653 shallow trade wind cumulus cloudiness and mass flux. *Journal of Geophysical*
654 *Research: Atmospheres*, 120(12), 6161–6178. doi: [https://doi.org/10.1002/](https://doi.org/10.1002/2014JD022950)
655 2014JD022950
- 656 Mieslinger, T., Horváth, Á., Buehler, S. A., & Sakradzija, M. (2019). The Depen-
657 dence of Shallow Cumulus Macrophysical Properties on Large-Scale Meteo-
658 rology as Observed in ASTER Imagery. *Journal of Geophysical Research:*
659 *Atmospheres*, 124(21), 11477–11505. doi: 10.1029/2019JD030768
- 660 Mlawer, E. J., Taubman, S. J., Brown, P. D., Iacono, M. J., & Clough, S. A. (1997).
661 Radiative transfer for inhomogeneous atmospheres: RRTM, a validated

- 662 correlated-k model for the longwave. *Journal of Geophysical Research: At-*
663 *mospheres*, 102(D14), 16663-16682. doi: 10.1029/97JD00237
- 664 Narenpitak, P., & Bretherton, C. S. (2019). Understanding negative subtropical
665 shallow cumulus cloud feedbacks in a near-global aquaplanet model using lim-
666 ited area cloud-resolving simulations. *Journal of Advances in Modeling Earth*
667 *Systems*, 11(6), 1600–1626. doi: 10.1029/2018MS001572
- 668 Nuijens, L., Medeiros, B., Sandu, I., & Ahlgrimm, M. (2015). Observed and mod-
669 eled patterns of covariability between low-level cloudiness and the structure of
670 the trade-wind layer. *Journal of Advances in Modeling Earth Systems*, 7(4),
671 1741-1764. doi: <https://doi.org/10.1002/2015MS000483>
- 672 Nuijens, L., Serikov, I., Hirsch, L., Lonitz, K., & Stevens, B. (2014). The distribu-
673 tion and variability of low-level cloud in the North Atlantic trades. *Quarterly*
674 *Journal of the Royal Meteorological Society*, 140(684), 2364-2374. doi: [https://](https://doi.org/10.1002/qj.2307)
675 doi.org/10.1002/qj.2307
- 676 Pincus, R., Fairall, C. W., Bailey, A., Chen, H., Chuang, P. Y., de Boer, G.,
677 ... Zuidema, P. (2021). Observations from the NOAA P-3 aircraft dur-
678 ing ATOMIC. *Earth System Science Data Discussions*, 2021, 1–25. doi:
679 10.5194/essd-2021-11
- 680 Quinn, P. K., Thompson, E., Coffman, D. J., Baidar, S., Bariteau, L., Bates, T. S.,
681 ... Zuidema, P. (2020). Measurements from the *RV Ronald H. Brown*
682 and related platforms as part of the Atlantic Tradewind Ocean-Atmosphere
683 Mesoscale Interaction Campaign (ATOMIC). *Earth System Science Data*
684 *Discussions*, 2020, 1–41. doi: 10.5194/essd-2020-331
- 685 Rasp, S., Schulz, H., Bony, S., & Stevens, B. (2020). Combining crowd-sourcing
686 and deep learning to explore the meso-scale organization of shallow convection.
687 *Bulletin of the American Meteorological Society*, 101(11), E1980–E1995. doi:
688 10.1175/BAMS-D-19-0324.1
- 689 Rauber, R. M., Stevens, B., Ochs, H. T., Knight, C., Albrecht, B. A., Blyth, A. M.,
690 ... Zuidema, P. (2007). Rain in shallow cumulus over the ocean: The rico
691 campaign. *Bulletin of the American Meteorological Society*, 88(12), 1912 -
692 1928. doi: 10.1175/BAMS-88-12-1912
- 693 Rolph, G., Stein, A., & Stunder, B. (2017). Real-time Environmental Applica-
694 tions and Display sYstem: READY. *Environmental Modelling and Software*,

- 695 95, 210-228. doi: <https://doi.org/10.1016/j.envsoft.2017.06.025>
- 696 Seifert, A., & Heus, T. (2013). Large-eddy simulation of organized precipitating
697 trade wind cumulus clouds. *Atmospheric Chemistry and Physics*, 13(11),
698 5631–5645. doi: 10.5194/acp-13-5631-2013
- 699 Siebesma, a. P., Bretherton, C. S., Brown, A., Chlond, A., Cuxart, J., Duynkerke,
700 P. G., ... Stevens, D. E. (2003). A large eddy simulation intercomparison
701 study of shallow cumulus convection. *Journal of the Atmospheric Sciences*,
702 60(10), 1201–1219. doi: 10.1175/1520-0469(2003)60<1201:ALESIS>2.0.CO;2
- 703 Stein, A. F., Draxler, R. R., Rolph, G. D., Stunder, B. J. B., Cohen, M. D., & Ngan,
704 F. (2015). NOAA’s HYSPLIT Atmospheric Transport and Dispersion Mod-
705 eling System. *Bulletin of the American Meteorological Society*, 96(12), 2059 -
706 2077. doi: 10.1175/BAMS-D-14-00110.1
- 707 Stevens, B., Bony, S., Brogniez, H., Hentgen, L., Hohenegger, C., Kiemle, C., ...
708 Zuidema, P. (2020). Sugar, gravel, fish and flowers: Mesoscale cloud patterns
709 in the trade winds. *Quarterly Journal of the Royal Meteorological Society*,
710 146(726), 141–152. doi: 10.1002/qj.3662
- 711 Stevens, B., Bony, S., Farrell, D., Ament, F., Blyth, A., Fairall, C., ... Zöger, M.
712 (2021). EUREC⁴A. *Earth System Science Data Discussions*, 2021, 1–78. doi:
713 10.5194/essd-2021-18
- 714 Vial, J., Vogel, R., Bony, S., Stevens, B., Winker, D. M., Cai, X., ... Brogniez,
715 H. (2019). A new look at the daily cycle of trade wind cumuli. *Jour-
716 nal of Advances in Modeling Earth Systems*, 11(10), 3148-3166. doi:
717 <https://doi.org/10.1029/2019MS001746>
- 718 Vogel, R., Bony, S., & Stevens, B. (2020). Estimating the shallow convective mass
719 flux from the subcloud-layer mass budget. *Journal of the Atmospheric Sci-
720 ences*, 77(5), 1559–1574. doi: 10.1175/jas-d-19-0135.1
- 721 Zelinka, M. D., Zhou, C., & Klein, S. A. (2016). Insights from a refined decomposi-
722 tion of cloud feedbacks. *Geophysical Research Letters*, 43, 9259–9269. doi: 10
723 .1002/2016GL069917
- 724 Zhang, M., Bretherton, C. S., Blossey, P. N., Austin, P. H., Bacmeister, J. T., Bony,
725 S., ... Zhao, M. (2013). CGILS: Results from the first phase of an interna-
726 tional project to understand the physical mechanisms of low cloud feedbacks in
727 single column models. *Journal of Advances in Modeling Earth Systems*, 5(4),

728 826–842. doi: 10.1002/2013MS000246

729 Zuidema, P., Torri, G., Muller, C., & Chandra, A. (2017). A Survey of Precipitation-

730 Induced Atmospheric Cold Pools over Oceans and Their Interactions with the

731 Larger-Scale Environment. *Surveys in Geophysics*, 38(6), 1283–1305. doi:

732 10.1007/s10712-017-9447-x

Supporting Information for "From Sugar to Flowers: A Transition of Shallow Cumulus Organization During ATOMIC"

DOI: 10.1002/

Pornampai Narenpitak^{1,2}, Jan Kazil^{1,2}, Takanobu Yamaguchi^{1,2}, Patricia

Quinn³, Graham Feingold²

¹Cooperative Institute for Research in Environmental Sciences, University of Colorado Boulder, Boulder, Colorado, USA

²National Oceanic and Atmospheric Administration, Chemical Sciences Laboratory, Boulder, Colorado, USA

³National Oceanic and Atmospheric Administration, Pacific Marine Environmental Laboratory, Seattle, Washington, USA

Additional Supporting Information (Files uploaded separately)

- Captions for Movies S1 to S3

Introduction

This is the Supporting Information (SI) for the manuscript "From Sugar to Flowers: A Transition of Shallow Cumulus Organization During ATOMIC," which contains the captions for Movies S1 to S3.

Additional Supporting Information (Files uploaded separately)

Movies S1 to S3

- **Movie S1:** An animation of hourly satellite images from the Geostationary Operational Environmental Satellite-16 (GOES-16) displaying the region of the trade cumulus organization transition from 8 UTC on February 2, 2020 to 2 UTC on February 3, 2020. The yellow dots represent hourly coordinates of the airmass-following trajectory on which the Lagrangian simulation is based. The red boxes indicate the simulation's $(192\text{-km})^2$ domain extent, which passes over the Ronald H. Brown research ship (RHB) or 54.5°W and 13.9°N (green '×') at 17 UTC.

- **Movie S2:** An animation of cloud and rain optical depths from the control simulation (CTL). The snapshots are plotted every minute from 10 UTC on February 2, 2020 to 2 UTC on February 3, 2020.

- **Movie S3:** As in Movie S2 but for the weaker vertical velocity simulation (WeakW).